

ALGORITHM THEORETICAL BASIS DOCUMENT

**AIRS-Team Retrieval For Core Products  
and Geophysical Parameters:  
Versions 6 and 7  
Level 2**

**Joel Susskind, GSFC, John Blaisdell, SAIC/GSFC, Lena Iredell,  
Adnet/GSFC, Jae Lee, GSFC, Adam Milstein, MIT Lincoln Laboratory,  
Chris Barnet, Science and Technology Corp., Evan Fishbein, JPL,  
Evan Manning, JPL, Larrabee Strow, UMBC**

**Joao Teixeira, JPL  
AIRS Team Leader**

**Editors:  
Eric J. Fetzer, Qing Yue, Heidar Th. Thrastarson,  
and Alexander Ruzmaikin, JPL**



Jet Propulsion Laboratory  
California Institute of Technology  
Pasadena, California

5 August 2020  
Document Version 2.0

## Table of Contents

EXECUTIVE SUMMARY .....	5
1. INTRODUCTION .....	7
1.1. Atmospheric Infrared Sounder (AIRS) Instrument and Retrieval Algorithm .....	7
1.2 AIRS Level 2 Data Products .....	11
1.3 Differences Between Earlier Retrieval Versions and Versions 6 and 7 .....	11
1.4 Differences between Versions 6 and Version 7 .....	13
1.5 Version History .....	15
1.6 Related Documents .....	15
2. RADIATIVE TRANSFER OF THE ATMOSPHERE (THE FORWARD PROBLEM) .....	18
2.1. Atmospheric Radiative Transfer in the Microwave.....	18
2.1.1 Oxygen .....	18
2.1.2. Water Vapor.....	19
2.1.3. Liquid Water.....	20
2.1.4. Microwave Rapid Transmittance Algorithm .....	21
2.1.5. Microwave Surface Brightness Model.....	25
2.2. Radiative Transfer of the Atmosphere in the Infrared .....	27
2.2.1. AIRS Atmospheric Layering Grid.....	31
2.2.2. Fast Transmittance Modeling .....	31
2.2.3. Spectroscopy .....	39
2.2.4. Monochromatic Transmittance Calculations .....	41
2.2.5. Spectral Response Function Measurements and Modeling .....	43
2.2.6 AIRS-RTA Error Analysis.....	45
3. RETRIEVAL METHODOLOGY.....	47
3.1 Steps in the Retrieval Methodologies Used in Version 6 and 7. ....	47
3.2 Channels Used in the Retrieval Steps .....	48
3.3 Initial Guess .....	49
3.3.1. SCC/NN Algorithm.....	50
3.3.2 Differences between Version 7 and Version 6 SCCNN .....	56
3.4 Clear-Column Radiances .....	56
3.5 Surface Parameter Retrieval Methodology .....	60
3.7. Difference Between Surface Skin Temperature and Surface Air Temperature .....	62

## AIRS V6 & V7 L2 ATBD

<b>3.8. Retrieval of Cloud Fraction and Cloud Top Pressure .....</b>	<b>63</b>
<b>3.9. Computation of Outgoing Longwave Radiation and Clear-Sky OLR.....</b>	<b>65</b>
<b>4. ERROR ESTIMATES AND QUALITY CONTROL FLAGS.....</b>	<b>68</b>
<b>APPENDIX: ABBREVIATIONS AND ACRONYMS.....</b>	<b>70</b>
<b>REFERENCES .....</b>	<b>73</b>

---

The research was carried out at the Jet Propulsion Laboratory, California Institute of Technology, under a contract with the National Aeronautics and Space Administration (80NM0018D0004).

Copyright 2020. All rights reserved.

## List of Figures and Tables

TABLE 1.1. GEOPHYSICAL QUANTITIES PRODUCED BY THE AIRS PROCESSING SOFTWARE USING ALGORITHMS DESCRIBED IN THIS DOCUMENT.....	7
FIGURE 1.1 AIRS LEVEL 2 PROCESSING FLOWCHART. BLUE BOXES (MW STEPS) APPLY ONLY TO THE AIRS/AMSU AND AIRS/AMSU/HSB SYSTEMS AND ARE OMITTED IN THE V7 IR-ONLY SYSTEM. IN THE LIGHT BLUE BOXES (IR/MW STEPS), EXCEPT IN THE NEURAL NETWORK STEP, THE V7 IR-ONLY SYSTEM OMITTS ANY USE OF THE MW CHANNELS. LIGHT GRAY BOXES REFER TO CLOUD PRESSURE AND FRACTION RETRIEVALS. DARK GRAY BOXES INDICATE THE CLOUD CLEARING STEPS. THE RED BOX INDICATES THE MAIN OUTPUTS FROM THE RETRIEVALS. THE YELLOW BOXES OCCUR IN POST-PROCESSING STEPS.....	10
TABLE 1.2 GEOPHYSICAL QUANTITIES PRODUCED BY POST-PROCESSING OF QUANTITIES GENERATED BY THE ALGORITHM DESCRIBED IN THIS DOCUMENT. THE PRODUCTION OF THESE PARAMETERS IS NOT DISCUSSED IN THIS DOCUMENT.....	11
FIGURE 2.1.1. MILLIMETER-WAVE PROPAGATION MODEL EXAMPLE.....	19
FIGURE 2.1.2. OXYGEN BAND WEIGHTING FUNCTIONS FOR UNIT SURFACE EMISSIVITY, WITH LABELS SHOWING AMSU CHANNEL NUMBER.....	24
FIGURE 2.1.3. WATER VAPOR WEIGHTING FUNCTIONS FOR UNIT SURFACE EMISSIVITY (LEFT) AND VAPOR BURDEN VS. PRESSURE IN THREE DIFFERENT CLIMATOLOGIES (RIGHT), FOR THE LABELLED CHANNELS.....	24
FIGURE 2.1.4. BRIGHTNESS TEMPERATURE ERRORS (RAPID ALGORITHM MINUS LINE-BY-LINE ALGORITHM) FOR AMSU AND HSB CHANNELS. VERTICAL LINES INDICATE $\pm 1$ STANDARD DEVIATION; $\varepsilon$ IS THE SURFACE EMISSIVITY.....	25
FIGURE 2.1.5. STATISTICS OF DIFFERENCES BETWEEN MEASURED BRIGHTNESS TEMPERATURES AND BRIGHTNESS TEMPERATURES CALCULATED FROM RADIOSONDE PROFILES. THREE PROFILE ENSEMBLES ARE SHOWN FOR HSB.....	26
FIGURE 2.2.1. SIMULATED MONOCHROMATIC (BLUE) AND AIRS SRF CONVOLVED (RED) BRIGHTNESS TEMPERATURE SPECTRA. THE RED CIRCLES INDICATE THE ACTUAL AIRS CHANNEL CENTROIDS.....	29
FIGURE 2.2.2. FLOW DIAGRAM FOR DEVELOPMENT OF THE AIRS-RTA.....	30
FIGURE 2.2.3. MEAN PRESSURE OF THE AIRS-RTA 100 LAYERS.....	32
FIGURE 2.2.4. RMS ERROR ESTIMATES OF THE AIRS-RTA MODEL.....	37
FIGURE 2.2.5. HISTOGRAM OF THE AIRS-RTA MODEL FITTING ERRORS FOR ALL CHANNELS.....	37
FIGURE 2.2.6. OPTICAL DEPTH TUNING USED IN THE VERSION 4 AND LATER AIRS-RTA. THE BOTTOM PANEL SHOWS THE SAME DATA AS THE TOP PANEL, BUT WITH THE VERTICAL RANGE EXPANDED TO ILLUSTRATE THE LARGE ADJUSTMENT TO THE WATER CONTINUUM IN THE SHORTWAVE CHANNELS.....	40
FIGURE 2.2.7. COMPARISON OF OBSERVED - CALCULATED BRIGHTNESS TEMPERATURES WITH AND WITHOUT OPTICAL DEPTH TUNING.....	41
FIGURE 2.2.8. ESTIMATED CHANGE TO AIRS OBSERVED BRIGHTNESS TEMPERATURES DUE TO THE OFFSET IN FRINGE POSITION IN NOVEMBER 2003.....	44
FIGURE 2.2.9. CENTROID DRIFT VERSUS TIME AND LATITUDE, FOR ASCENDING (DAY) ORBITS.....	45
FIGURE 2.2.10. BRIGHTNESS TEMPERATURE ERROR FOR A 0.5% ERROR IN CHANNEL CENTROIDS.....	46
TABLE 2.2.1. AIRS-RTA ERROR ESTIMATES.....	46
FIGURE 3.2.1. CHANNELS USED IN THE RETRIEVALS OF THE GEOPHYSICAL VARIABLES.....	48
FIGURE 3.3.1. SCHEMATIC OF STOCHASTIC CLOUD CLEARING / NEURAL NETWORK (SCC/NN).....	49
FIGURE 3.3.2. SCHEMATIC OF STOCHASTIC CLOUD CLEARING ALGORITHM.....	51
FIGURE 3.3.3. SCHEMATIC OF PPC-NN, THE COMBINATION OF COMPRESSION AND NEURAL NETWORK ALGORITHMS.....	53

## EXECUTIVE SUMMARY

This document provides the theoretical and analytical basis for the fundamental radiative transfer and retrieval algorithms used to generate Atmospheric Infrared Sounder (AIRS) retrieved quantities in the Version 6 and Version 7 product release. These algorithms process radiances observed by AIRS and also by the Advanced Microwave Sounder (AMSU) and the Humidity Sounder for Brazil (HSB).

The basic ‘Core’ quantity retrieved by the AIRS system is cloud cleared radiance, an estimate of spectrally-resolved radiances from the cloud-free part of the scene, or in the case of thin clouds, radiance in the absence of clouds. After an initialization using a neural network, other quantities are retrieved by matching cloud cleared radiances to forward modelled radiances. These retrieved quantities include estimates of atmospheric temperature, water vapor and trace gases, along with a set of cloud top properties, and surface properties. The radiative transfer forward model used in the retrieval algorithm requires high vertical resolution. Consequently, the output of the Core retrieval algorithm is resolved into 100 layers though the true information content is considerably coarser than this. This document describes the three basic steps of cloud clearing, initialization with a neural network, and the final retrieval.

The AIRS/AMSU/HSB instruments have been on orbit for over 18 years (as of mid 2020). They have provided a data record of over 19 billion AIRS spectra. The AIRS radiance and retrieved data sets are available in a very large (and sometime complex) data archive. Supporting the AIRS record is an extensive set of documentation, and over 1,000 peer-reviewed papers. AIRS data users should become familiar with these other sources of documentation. These provide a more complete picture of the AIRS system than is provided here, and are discussed in Section 1.6 below.

Some aspects of the AIRS processing system are not included in this document, as they are not fundamental to the Core algorithms. The reduction of resolution, from 100 layers to a few dozen levels representing a conservative estimation of the true vertical resolution of the retrieved quantities, is discussed in the document *AIRS Version 7 Product Levels, Layers, and Trapezoids*). Also not discussed are post-processors to the Core algorithm generating estimates of cloud effective radius and phase, the amounts of carbon

dioxide, and ammonia. Similarly, flags indicating the presence of dust and sulfur dioxide are set by radiance brightness temperature differences. These product generation algorithms are described in detail in other documents. Finally, this document does not describe the organization of the many datasets produced by the algorithms described here. See Section 1.6 below for a list of AIRS documentation, and *Overview of the AIRS Mission: Instruments, Processing Algorithms, Products and Documentation* for an introduction to AIRS data products.

# 1. INTRODUCTION

## 1.1. Atmospheric Infrared Sounder (AIRS) Instrument and Retrieval Algorithm

This document describes the algorithm to generate Atmospheric Infrared Sounder (AIRS) Science Team temperature and humidity profiles, surface and cloud properties, and trace gases amounts describing the geophysical state of the atmosphere and the surface (see Table 1.1 below). These geophysical quantities constitute the ‘Core Products’ in the title of this document. Other quantities are generated by post-processors to the algorithm described here. Those are listed in Table 1.2 below, and the algorithms to generate them are listed in Section 3. The Core algorithm also produces ancillary information such as quality flags and estimates of profile vertical resolution (averaging kernels). These are discussed in Section 4, or in supporting documents listed in Section 1.6, as appropriate.

Retrieved Quantity	Physical Characteristics
Cloud Cleared IR Radiance	Spectrally resolved radiance from cloud-free FOVs.
Sea Surface Temperature	Surface property
Land Surface Temperature	Surface property
Land Surface Emissivity	Surface property
Temperature Profile	Height-resolved, surface to mesosphere
Water Vapor Profile	Height-resolved, surface to upper troposphere
Total Precipitable Water	Total water in retrieved water vapor profile
Fractional Cloud Cover	Cloud top property
Cloud Top Height	Cloud top property
Cloud Top Temperature	Cloud top property
Ozone Profile	Height-resolved, upper troposphere to mesosphere
Total Ozone	Total ozone in retrieved ozone profile
Carbon Monoxide	Amount in middle troposphere
Methane	Amount in middle to upper troposphere
Outgoing Longwave Radiation	Radiative flux derived from spectrally resolved radiances

**Table 1.1. Geophysical quantities produced by the AIRS processing software using algorithms described in this document.**

AIRS is a cross-track scanning, high spectral resolution infrared sounder onboard the NASA Aqua satellite collecting radiance data with a 13.5 km spatial resolution in the horizontal at nadir. It has 2378 infrared channels. Because of its wide scan swath, AIRS is

an imaging hyperspectral sounder, covering 80% of the globe twice per day, during the ascending (day) and the descending (night) overpasses. However, the images are in scan coordinates along the orbit track (skewed in latitude and longitude), with considerable overlap at high latitudes and gaps near the equator.

The AIRS instrument was designed to work in tandem with two co-registered microwave instruments: the Advanced Microwave Sounding Unit-A (AMSU-A, or simply AMSU) and the Humidity Sounder for Brazil (HSB). HSB stopped operating on 6 February 2003. One configuration of the retrieval algorithm processes the short AIRS/AMSU/HSB record. AMSU on Aqua has steadily lost channels sensitivity to surface and near-surface properties beginning in 2011, with significant loss on September 24, 2017. Another configuration of the retrieval algorithm processes the AIRS/AMSU record, particularly from 2002 through 2017. A third configuration of the retrieval algorithm processes AIRS-only radiances. This configuration is intended to provide a consistent record from the inception of AIRS observations on 30 August 2002 through end AIRS operations.

This document describes both the AIRS Science Team Version 6 and Version 7 retrieval algorithms. (Their differences are described in Section 1.4 below.) The Version 6 and 7 retrieval algorithms generate surface and atmospheric parameters using AIRS radiance observations taken within a 3×3 array of AIRS Fields of View (FOVs) contained within an AMSU footprint, called an AIRS Field of Regard (FOR). HSB radiances, when available, are co-registered with AIRS FOVs. Retrievals of most geophysical parameters are performed at AIRS FOR horizontal resolution of about 45 km at nadir. Cloud products are retrieved at AIRS FOV horizontal resolution of 13.5 km at nadir. The Version 6 and Version 7 retrieval process consists of four major components, repeated iteratively (see Figure 1.1):

1. ***The First Guess.*** The first guess uses observed AIRS radiances within the AIRS FOR, and a neural network, to generate the initial guess  $X_0$  to start the retrieval process.
2. ***Cloud Clearing.*** The second algorithm component retrieves clear column radiances  $\hat{R}_i$  in the FOR for all channels, which are updated as part of the overall retrieval process.  $\hat{R}_i$  is a derived quantity representing the radiance channel  $i$  would have observed if the AIRS FOR were cloud-free.



3. ***The Physical Retrieval.*** The third retrieval component is a multi-step, physically based procedure, starting with the initial guess  $X_0$ , that finds geophysical parameters which best match both the observed AMSU radiances and AIRS clear column radiances  $\hat{R}_i$  for those channels used in a given step of the retrieval process. Retrieval steps are done sequentially and determine the following geophysical parameters: surface skin temperature, surface spectral emissivity, surface bidirectional reflectance; atmospheric temperature profile, atmospheric moisture profile, ozone profile, and mid-tropospheric methane and carbon monoxide within an AIRS FOR, as well as the cloud fraction (the product of areal coverage and emissivity) and cloud top pressure in each AIRS FOV. These steps are done sequentially so as to make the retrieval process as linear as possible in each step, and to allow for use of a set of channels in each retrieval step whose radiances are most sensitive to what is being solved for in that step and parameters previously solved for, while also being relatively insensitive to geophysical parameters not yet solved for.

4. ***Quality Control.*** The fourth retrieval component derives error estimates for retrieved geophysical parameters, and uses these error estimates to generate case-dependent quality control (QC) flags for retrieved geophysical parameters.

In the following document we present the theoretical basis of the AIRS Level 2 algorithm. The overall flow of the retrieval is shown in Figure 1.1.

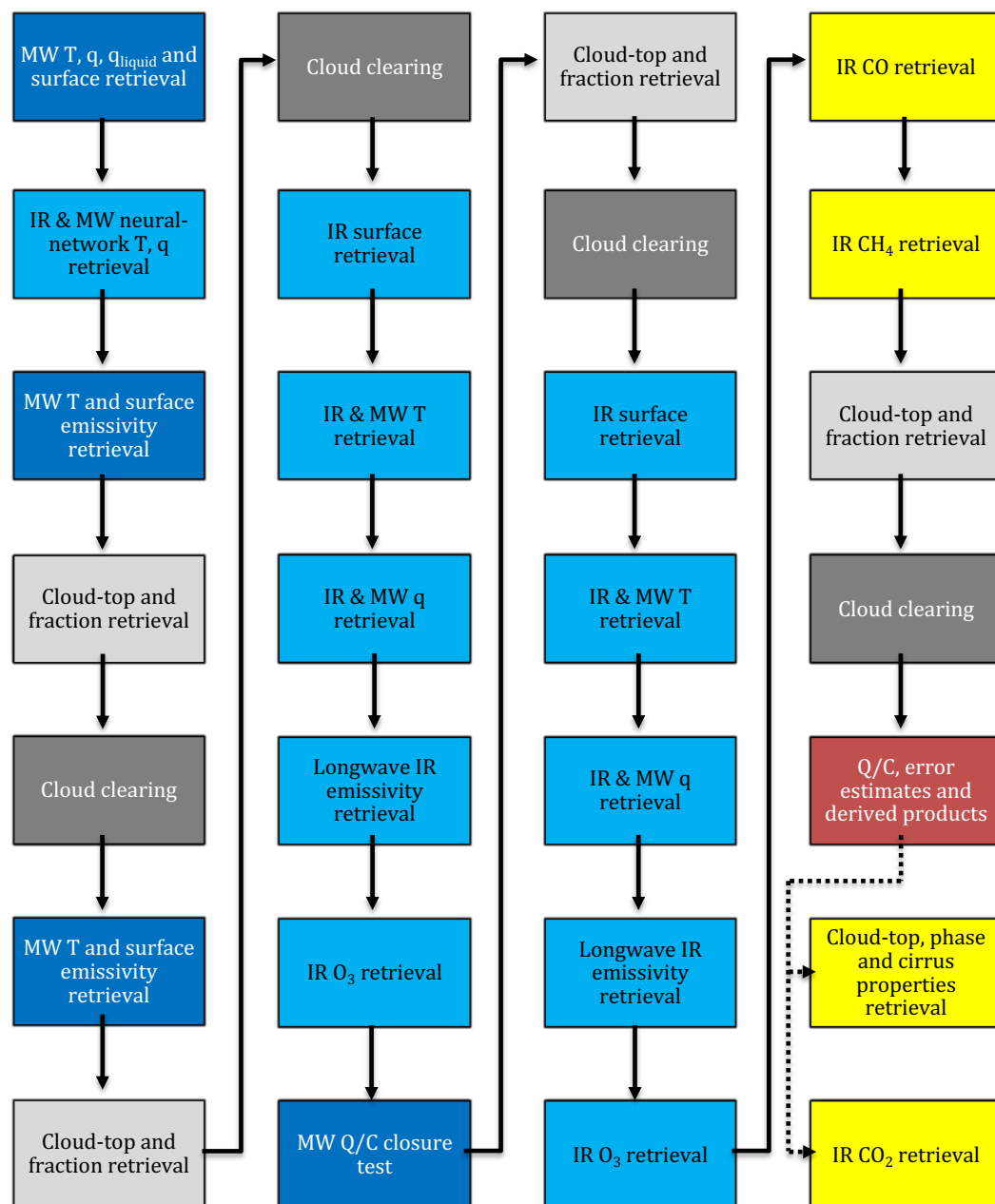


**Figure 1.1 AIRS Level 2 processing flowchart.** Blue boxes (MW steps) apply only to the AIRS/AMSU and AIRS/AMSU/HSB systems and are omitted in the V7 IR-only system. In the light blue boxes (IR/MW steps), except in the neural network step, the V7 IR-only system omits any use of the MW channels. Light gray boxes refer to cloud pressure and fraction retrievals. Dark gray boxes indicate the cloud clearing steps. The red box indicates the main outputs from the retrievals. The yellow boxes occur in post-processing steps.

## 1.2 AIRS Level 2 Data Products

Table 1.1 lists the geophysical quantities retrieved by the AIRS Level 2 Product Generation Executive (PGE) software implementation of the algorithm described in this document. Table 1.2 lists additional quantities produced by post-processing of parameters listed in Table 1.1, but also as part of PGE processing. The generation of quantities in Table 1.2 will not be discussed in this document; see related documents in Section 1.6. Creation of all versions of Level 2 is performed at the Goddard Earth Sciences Data and Information Services Center (GES DISC).

Retrieved Quantity	Physical Characteristics
Cloud Phase	Cloud top property
Cloud Effective Radius	Cloud top property
Carbon Dioxide	Amount in middle troposphere
Ammonia	Total amount

**Table 1.2 Geophysical quantities produced by post-processing of quantities generated by the algorithm described in this document. The production of these parameters is not discussed in this document.**

## 1.3 Differences Between Earlier Retrieval Versions and Versions 6 and 7

AIRS Version 5 and earlier used as its first guess a regression solution based on radiosonde observations (see *AIRS Algorithm Theoretical Basis Document, AIRS-Team Retrieval For Core Products and Geophysical Parameters, Level 2, JPL D-17006, Version 4.0, 1 March 2007*). AIRS Version 6 and Version 7 algorithms use a Stochastic Cloud Clearing Neural Network (SCCNN) algorithm to obtain the first guess of surface skin temperature, temperature and water vapor profiles using radiance observations from AIRS and AMSU and trained on the ECMWF model analysis. (They are also distributed to users in the Level 2 support product as “TAirSCCNN”, “H2OCDSCCNN”, and “TSurfSCCNN”.) The algorithm consists of two key parts: SCC (Stochastic Cloud Clearing) estimates the cloud-cleared infrared spectrum using series of linear and nonlinear operations on AIRS/AMSU radiances within an AIRS field of view. The NN (neural network) estimates temperature and water vapor profiles from projected principal components of the cloud-cleared spectrum. More details on the SCCNN algorithm are presented in Section 3.3. The validation and evaluation of the SCCNN for Version 6 and

Version 7 can be found in the *AIRS Version 7 Level 2 Performance Test and Validation Report*.

The basic cloud clearing and physical retrieval methodologies used in the AIRS Science Team Version 6 and 7 retrieval algorithms, including the meaning and derivation of Jacobians, the channel noise covariance matrix, and constraints of the background term, are essentially identical to those of the AIRS Science Team pre-launch algorithm described in Susskind et al. (2003), which was developed and tested using simulated AIRS/AMSU observations. No explicit weight is given in the Version 6 physical retrieval to either an a-priori state or the initial guess since the AIRS cost function does not include these terms. (See Rogers (2000) for a discussion of optimal estimation-based retrieval methods that include weighted priors in the cost function.) However, in order to reduce the spurious humidity retrievals near the surface, Version 7 increases the damping on water vapor retrievals which gives the SCCNN first guess greater weight relative to the physical retrieval than in Version 6. Susskind et al. (2006) describe the AIRS Science Team Version-4 retrieval algorithm implemented by the Goddard DAAC (Distributed Active Archive Center), —the PGE as discussed above— to process AIRS/AMSU observations from September 2002 (when the AIRS instrument became stable) through September 2007, two months after AIRS Version 5 processing began. The AIRS Science Team AIRS/AMSU Version 4 retrieval and cloud clearing algorithms included new terms to account for systematic and random errors made in the computations of expected channel radiances for a given geophysical state using the Version-4 AIRS and AMSU Radiative Transfer Algorithm (RTA's). Susskind et al. (2006) also introduced a QC concept that generated different QC flags for a given profile as a function of height, and had separate QC flags related to surface skin temperature. This new methodology was used in Versions 5, 6, and 7 to generate profile-by-profile, level-by-level, temperature error estimates and QC parameters. The AIRS Science Team Version 5 retrieval algorithm (Susskind et al., 2011) applied a new set of channels used to retrieve the atmospheric temperature profile.

The physical retrieval and cloud clearing steps in the AIRS Version 6 and 7 retrieval algorithm contain additional improvements. Foremost among these is the methodology to determine surface skin temperature and surface spectral emissivity from AIRS radiance observations. There have also been significant improvements to the QC methodology for

different geophysical parameters, to the methodology to generate first guesses for atmospheric and surface parameters, and to the methodology to determine cloud parameters and derive outgoing longwave radiation (OLR) from the AIRS/AMSU observations.

Version 6 and 7 have an “AIRS-Only” (AO) processing capability which utilizes only AIRS radiance observations. Version 6 AO produces only slightly degraded global performance than that obtained utilizing both AIRS and AMSU observations, though the loss of AMSU may affect performance locally, especially in cloudier and frozen surface conditions (Yue and Lambrigtsen, 2017). In Version 7 AO algorithms, the ambiguity in differentiating frozen and non-frozen surface classification in the infrared-only algorithm has been removed by using ice concentration over ocean and water equivalent accumulated snow depth over land obtained from the ancillary Global Forecasting System (GFS) files. The Version 7 AO algorithm also uses a new SCCNN first guess that utilizes stable microwave channels of AMSU-A1, while its physical retrieval step uses infrared channels only and does not use microwave information. This “AIRS Only” capability is an important processing mode with the loss of AMSU-A2 in September, 2016. The AO retrieval allows a consistent algorithm to be applied across the entire AIRS record.

#### ***1.4 Differences between Versions 6 and Version 7***

The AIRS Science Team Version 6 retrieval algorithm is described in great detail in Susskind et al (2014a). The differences between Version 6 and Version 7 algorithms are summarized in this section and also described in detail in the *AIRS Version 7 Level 2 Performance Test and Validation Report*. The major changes between the two versions include:

- 1) Changes to first guess:
  - a. Version 7 has an improved SCCNN first guess for surface temperature, atmospheric temperature and humidity profiles;
  - b. A new climatological first guess was developed for ozone, separating ozone hole cases from other cases to yield two distinct profile shapes over Antarctica during spring, based on the 50 hPa temperature given by the SCCNN.
- 2) Multiple changes to the channel selection in the physical retrieval:

## AIRS V6 & V7 L2 ATBD

- a. The shortwave channels in the range of 2607~2657  $\text{cm}^{-1}$  are removed from the Version 7 water retrieval, which eliminated the spurious day-night bias reported in Version 6 water products;
  - b. The strongest water lines were removed from the retrieval as their utilization had a detrimental effect. Water continuum channels were added to the water retrieval;
  - c. Seven additional 4  $\mu\text{m}$  channels were added to the temperature retrieval to increase information at the top of the atmosphere, which also affects the ozone retrieval;
  - d. The strongest ozone lines were added to the retrieval for Version 7 and two additional spectral hinge points in the 9.6  $\mu\text{m}$  region added to the surface retrieval for temperature, ozone, and water vapor;
  - e. Changes to surface classification in the IR-only retrieval algorithm;
  - f. Trapezoids were added for temperature, water vapor, and temperature retrievals. Please see *AIRS Version 7 Product Levels, Layers, and Trapezoids*.
- 3) Changes to the quality control procedure (see *AIRS/AMSU/HSB Version 7 Level 2 Quality Control and Error Estimation*):
- a. The error estimate used as the decision point for atmospheric temperature and water profile QCs is moved from 6 layers above the surface in Version 6 to 2 layers above the surface over frozen and land surfaces in Version 7. This effectively uses the entire profile error estimate information and allows the algorithm to make finer distinctions of quality over land and frozen areas near the surface.
  - b. The numerical threshold points for marking profile levels with QC=2 is tightened over land from the mid to lower atmosphere, and for frozen cases in the middle atmosphere, while the numerical threshold for frozen cases near the surface is slightly loosened which increases the yield over frozen surfaces.
  - c. Quality control specific to ozone was added in Version 7. The ozone retrieval is rejected under the following conditions: the attempted change

on the first iteration is too large indicating the temperature or water profiles may be in error; radiative closure is not achieved in the ozone channels; the dust test indicates the presence of significant dust; and/or the change in emissivity from the first guess is very different in the ozone spectral region and the adjacent spectral regions.

For more details, refer to the *AIRS Version 7 Level 2 Performance Test and Validation Report*.

### **1.5 Version History**

1. Version 2.1 (20 December 1999) of the AIRS Level 2 ATBD, ‘AIRS-Team Retrieval for Core Products and Geophysical Parameters,’ replaced the Version 1.7 (18 September 1997) document, ‘AIRS-Team Unified Retrieval for Core Products.’
2. Version 2.2 (26 April 2001) was the last pre-launch release of the Level 2 ATBD. This revision incorporated changes in response to the ATBD reviewers.
3. No Version 3.0 ATBD was issued.
4. The first post-launch Level 2 Algorithm Theoretical Basis Document (ATBD) was Version 4.0 (1 March 2007), named 4.0 to synchronize the numbering scheme with the version of the AIRS Product Generation Executive (PGE) that was delivered to the Goddard Space Flight Center (GSFC) Distributed Active Archive Center (DAAC) for routine AIRS data processing.
5. No Version 5.0 ATBD was issued.
6. This document describes Versions 6.0 and 7.0

### **1.6 Related Documents**

Many of the documents in the list below can be accessed at the AIRS documentation web page:

<https://disc.gsfc.nasa.gov/information/documents?title=AIRS%20Documentation>

#### ***Pre-Launch Documents:***

AIRS Science and Measurement Requirements Document, JPL D-6665, Rev. 1, September 1991, AIRS Brochure.

## AIRS V6 & V7 L2 ATBD

AIRS Project Algorithm Theoretical Basis Document, Level 1b, Part 2: Microwave Instruments, JPL D-17005, Version 1.2, 15 November 1996.

AIRS Instrument Calibration Plan, JPL D-16821, Preliminary, 14 October 1997.

AIRS Team Science Data Validation Plan, Core Products, JPL D-16822, Version 1.2, 15 August 1997.

AIRS Algorithm Theoretical Basis Document, AIRS-Team Unified Retrieval For Core Products, Level 2, JPL D-17006, Version 1.7, 18 September 1997

AIRS Algorithm Theoretical Basis Documents, Level 1B, Part 1: Infrared Spectrometer, JPL D-17003, Version 2.0, 4 January 1999.

AIRS Algorithm Theoretical Basis Document, Level 1B, Part 2: Visible/Near-Infrared Channels, JPL D-17004, Version 2, 4 January 1999.

AIRS Algorithm Theoretical Basis Document, AIRS-Team Retrieval For Core Products and Geophysical Parameters, Level 2, JPL D-17006, Version 2.1, 20 December 1999

AIRS Algorithm Theoretical Basis Document, Level 1B, Part 2: Visible/Near-Infrared Channels, JPL D-17004, Version 2.2, 10 November 2000.

AIRS Project Algorithm Theoretical Basis Document, Level 1b, Part 2: Microwave Instruments, JPL D-17005, Version 2.1, 10 November 2000.

AIRS Algorithm Theoretical Basis Documents, Level 1B, Part 1: Infrared Spectrometer, JPL D-17003, Version 2.2i, 10 November 2000.

AIRS Team Science Data Validation Plan, JPL D-16822, Version 2.1.1, 5 June 2000.

AIRS Algorithm Theoretical Basis Document, AIRS-Team Retrieval For Core Products and Geophysical Parameters, Level 2, JPL D-17006, Version 2.2, 26 April 2001.

AIRS Visible and Infrared In-Flight Calibration Plan, JPL D-18816, Version 3.0, June 2002.

### ***Post-Launch Documents, Version 5 and Earlier:***

AIRS Level 1B Visible, Infrared and Telemetry Algorithms and Quality Assessment (QA) Processing Requirements, JPL D-20046, Version 2.2, 14 February 2003.



## AIRS V6 & V7 L2 ATBD

AIRS Algorithm Theoretical Basis Document, Level 1B, Part 1: Infrared Spectrometer, JPL D-17003, Version 4.0, 1 March 2007.

AIRS Algorithm Theoretical Basis Document, AIRS-Team Retrieval For Core Products and Geophysical Parameters, Level 2, JPL D-17006, Version 4.0, 1 March 2007.

### ***Version 6 and 7 Documents:***

[Overview of the AIRS Mission: Instruments, Processing Algorithms, Products and Documentation.](#) July, 2020.

[AIRS/AMSU/HSB Version 6 Level 2 Performance and Test Report.](#) November, 2017.

[AIRS Version 7 Level 2 Performance Test and Validation Report.](#) April, 2020.

[AIRS/AMSU/HSB Version 7 Retrieval Flow.](#) June, 2020.

[AIRS Version 7 Retrieval Channel Sets.](#) June, 2020.

[AIRS/AMSU/HSB Version 7 Changes from Version 6.](#) June, 2020.

[AIRS/AMSU/HSB Version 7 Level 2 Product Levels Layers and Trapezoids.](#)

[AIRS/AMSU/HSB Version 7 Level 2 Quality Control and Error Estimation.](#) June, 2020.

[AIRS/AMSU/HSB Version 7 Level 2 Product User Guide.](#) July, 2020.

## 2. RADIATIVE TRANSFER OF THE ATMOSPHERE (THE FORWARD PROBLEM)

The physical retrieval methodology described here depends on the ability to accurately and rapidly calculate the outgoing radiance from a prescribed state of the surface and the atmosphere. The following discusses the microwave (Section 2.1) and infrared (Section 2.2) radiative transfer and error estimates. Almost invariably, the statistical evaluation of calculated brightness temperatures, relative to those observed when the state of the atmosphere is reliably known, differs in the mean by a small, but significant amount, referred to as “bias.” This bias varies with frequency and may be a function of other parameters, such as the scan angle.

### 2.1. Atmospheric Radiative Transfer in the Microwave

At the frequencies measured by AMSU, the most important absorbing gases in the atmosphere are oxygen and water vapor. The oxygen molecule has only a magnetic dipole moment, and its spectral lines are intrinsically much weaker than those which result from the electric dipole of water vapor; however, the much greater abundance of oxygen in the atmosphere more than compensates for this difference. When clouds are present, liquid water also plays a role in radiative transfer. However, fair-weather cirrus composed of ice particles small compared to the wavelength are generally transparent to AMSU-A and HSB frequencies. (Note that HSB stopped operating on 6 February 2003. HSB is used in only one configuration of the Version 6 and 7 algorithms, for the period 30 August 2002 through 6 February 2003. This is a separately available product.)

#### 2.1.1 Oxygen

O<sub>2</sub> spin-rotation transitions comprise approximately thirty lines between 50 and 70 GHz and an isolated line at 118.75 GHz (which is not observed by AMSU or HSB). Several groups have measured the pressure-broadened widths of the lines in the 50-70 GHz band. The line parameters used for the forward model are from the Millimeter-wave Propagation Model (MPM92) (Liebe, *et al.*, 1992). The significant degree of line mixing of the oxygen microwave spectrum introduces difficulty for construction of radiative transfer models. In MPM92, line mixing was treated by a first-order expansion in pressure. The coefficients for this expansion were determined by a constrained linear fit to laboratory

measurements made on an  $O_2 - N_2$  mixture over the frequency range of 49-67 GHz and the temperature range 279-327 K, with a noise level of approximately 0.06 dB/km. Within that range, the model represents the measurements to  $\leq 0.2$  dB/km (see for example, Figure 2.1.1). It is possible that extrapolation to colder temperatures introduces larger errors. Measurements from the NASA ER-2 at 52-56 GHz (Schwartz, 1997) seem to be in agreement with the MPM92 model, however.

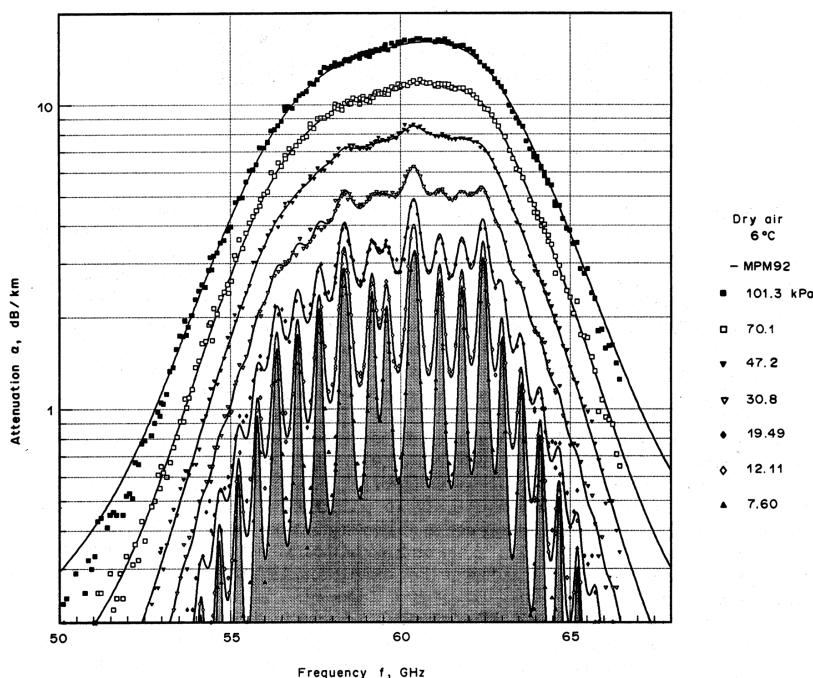


**Figure 2.1.1. Millimeter-wave propagation model example.**

### 2.1.2. Water Vapor

Water has a weak rotational line at 22.23 GHz that is semi-transparent at normal atmospheric humidity, and a much stronger, opaque line at 183.31 GHz. Intensities of these lines have been calculated and tabulated by Poynter and Pickett (1996 version of JPL line catalog) and Rothman, *et al.*, (1998) (HITRAN), among others. The HITRAN intensities are used here. For the 22-GHz line, the JPL intensity is higher than the HITRAN value by 0.3%. A measurement by Liebe, *et al.*, (1969) (estimated error 0.3%) is 3.5% lower than the HITRAN value. At 183 GHz, the JPL line intensity is 0.1% higher than HITRAN. Widths have been measured by Liebe, *et al.*, (1969) and Liebe and Dillon (1969) at 22 GHz with estimated uncertainty of 1% for both self and foreign-gas broadening; and by Bauer,

*et al.*, (1989) and Tretyakov, *et al.* (2003) at 183 GHz, with uncertainties of 0.5% for self-broadening and 1.0% for foreign-gas broadening, respectively. However, Gamache, *et al.*, (1994) concluded from a survey of measurements of many H<sub>2</sub>O lines that, in general, measured line widths should be considered to have uncertainties of 10-15%. The line at 183 GHz is a case in which published measurements of width differ significantly, but the value of Tretyakov, *et al.*, (2003), which is used here, lies near the centroid of the measurements.

At frequencies away from these two lines, microwave absorption by water vapor is predominantly from the continuum, which is attributed to the low-frequency wing of the intense infrared and submillimeter rotational band lines. In the microwave part of the spectrum, the foreign-broadened component of the continuum is stronger than the self-broadened component, for realistic atmospheric H<sub>2</sub>O mixing ratios. Measurements of continuum absorption as a function of temperature have been made at various frequencies by Liebe and Layton (1987), Godon, *et al.* (1992) and Bauer, *et al.* (1993, 1995). There are also numerous measurements at single temperatures and frequencies in the laboratory, and in the atmosphere where temperature and mixing ratio are variable. The measurements do not present an entirely consistent picture. Rosenkranz (1998) proposed that the most satisfactory overall agreement between laboratory and atmospheric measurements of the water continuum was obtained with a combination of the foreign-broadened component from MPM87 (Liebe and Layton, 1987) with the self-broadened component from MPM93 (Liebe, *et al.*, 1993). The combined model is used here.

### 2.1.3. Liquid Water

It is important to distinguish between precipitating and non-precipitating clouds with respect to their interactions with microwaves. Over the range of wavelengths measured by AMSU and HSB, non-precipitating droplets (with diameters of 50  $\mu$ m or less) can be treated using the Rayleigh small-droplet approximation. In this regime, absorption is proportional to the liquid water content of the air, and scattering can be neglected. The model for the dielectric constant limits the accuracy of these calculations. The double-Debye model of Liebe, *et al.*, (1991) is used here; for temperatures  $> 0$  °C, it has an estimated maximum prediction error of 3% between 5 and 100 GHz, and 10% up to 1 THz.

Although some measurements of static dielectric constant at temperatures as low as  $-20^{\circ}\text{C}$  were used by Liebe, *et al.* to develop their model, its use for supercooled water must be considered to be an extrapolation, with uncertain accuracy. (The model is implemented using the alternate eq. 2b in Liebe, *et al.*)

Precipitation, in contrast, requires Mie theory to calculate both absorption and scattering. The latter is generally not negligible, and is the dominant term at some wavelengths. In the case of convective storms, scattering from ice at high altitudes is often the most important process affecting microwaves. The rapid transmittance algorithm uses only the small-droplet approximation for cloud liquid water, and scattering is not included in it. For this reason, retrieved profiles with more than  $0.5 \text{ kg/m}^2$  cloud liquid water are probably rain-contaminated and rejected.

#### 2.1.4. Microwave Rapid Transmittance Algorithm

The physical retrieval algorithms used for AIRS/AMSU and AIRS/AMSU/HSB require radiative transfer calculations for each profile and hence need a computationally efficient transmittance algorithm. The microwave Rapid Transmittance Algorithm (RTA) computes an effective channel transmittance between two adjacent pressure levels as

$$\langle \tau(P_1, P_2) \rangle = \exp \left[ -(\alpha + \beta \rho_v + \gamma \rho_L) \right] \quad (2.1.1)$$

where  $\rho_v$  is the water vapor column density of the  $(P_1, P_2)$  layer,  $\rho_L$  is its liquid water column density, and the coefficients  $\alpha$ ,  $\beta$ ,  $\gamma$ , are calculated for each layer and channel. They implicitly depend on temperature, pressure, and the angle of observation;  $\beta$  also depends implicitly on  $\rho_v$ . For AMSU channel 14,  $\alpha$  has a weak dependence on the local geomagnetic field. The magnetic field is calculated by a fifth-order spherical-harmonic representation that has an accuracy of a few microteslas. The coefficient  $\alpha$  includes the opacity due to  $\text{O}_2$  and a small contribution from pressure-induced absorption by  $\text{N}_2$ . Parameterization of the coefficients uses approximations described by Rosenkranz (2003) for oxygen-band or window-type channels. In the oxygen band, effective layer opacities are represented by a polynomial in temperature. The opacity profile is computed on a set of fixed pressure levels and then linearly interpolated to the pressure levels of the retrieval, which can be variable (as is the case for the surface pressure). Window-channel coefficients

use analytic approximations for far-wing line and continuum absorption. Channels near the two water lines (AMSU channel 1 and HSB channels 3-5) use a Lorentzian-line calculation for the nearby line, with the contributions of other lines treated in the same way as for a window. The local water-line parameters, the water continuum, and the liquid-water absorption are interpolated from a table as functions of temperature.

The retrieval algorithm described in Section 3 also makes use of the derivatives  $d\alpha/dt$  and  $d\beta/d\rho_V$ , which are computed in the rapid algorithm by appropriate analytic expressions corresponding to the local-line and continuum components.

The transmittance of multiple layers is calculated by taking the product of the transmittances for each layer. This transmittance is then used in the radiative transfer equation to compute brightness temperature:

$$\Theta_{TOA} = \Theta_{direct} + \tau(0, P_s) \left[ \Theta_s + \Theta_{sky} \left( 1 - \frac{\Theta_s}{T_s} \right) \right] \quad (2.1.2)$$

where  $\Theta_{TOA}$  is the brightness temperature of microwave radiation emitted from the top of the atmosphere,  $\tau(0, P_s)$  is the one-way transmittance of the atmosphere,

$$\Theta_{direct} = \int_0^{P_s} T(P) < d\tau(0, P) > \quad (2.1.3)$$

is the component of brightness temperature emitted from the atmosphere on a direct path to space,  $\Theta_s$  is the surface brightness (emissivity times temperature),

$$\Theta_{sky} = \int_0^{P_s} T(P) < d\tau(P_s, P) > + \Theta_c < \tau(0, P_s) > \quad (2.1.4)$$

is the sky brightness temperature (including the attenuated cosmic contribution) as it would be observed from the surface, and  $T_s$  is the physical surface temperature.  $T(P)$  is atmospheric temperature at level  $P$ ,  $P_s$  is the surface pressure, and  $\Theta_c$  is the cosmic background brightness temperature and transmittance  $\tau$  is defined in equation (2.1.1). The form of (2.1.4) allows separation of the estimation of surface brightness from the estimation of temperature, as described in Section 2.1.5.

$\theta_{sky}$  is computed for a zenith angle  $\theta_{ref}$  which, due to surface scattering, differs from the zenith angle  $\theta$  for the direct path from surface to satellite. When the surface is classified as either water or coastline in the neural network initialization described in Section 3.3, the ratio  $\rho_s = \sec(\theta_{ref})/\sec(\theta)$  is estimated as part of the retrieval solution, as described in Section 3.6 (and different from the column density  $\rho_L$  in the previous section). For all other surface types, surface scattering is assumed to be Lambertian, and is approximated by

$$\sec(\theta_{ref}) = 1.55 - 0.16 \ln(\kappa_0 + 0.06) \quad (2.1.5)$$

where  $\kappa_0 = -\ln(\tau_{zenith}(0, P_s))$  is the opacity of the atmosphere at zenith.

Planck's equation for radiant intensity is a nonlinear function of temperature. For microwave frequencies, however, the physical temperatures encountered in the earth's atmosphere lie at the high-temperature asymptote of this function. Hence, as discussed by Janssen (1993), brightness temperature can be used as a surrogate for radiance in the equation of radiative transfer with an accuracy of a few hundredths of a Kelvin, provided that the cosmic background is assigned an effective brightness temperature at frequency  $\nu$  of

$$\Theta_C = \frac{h\nu}{2k} \times \frac{e^{\frac{h\nu}{kT_C}} + 1}{e^{\frac{h\nu}{kT_C}} - 1} \quad (2.1.6)$$

instead of its actual temperature  $T_C = 2.73$  K, in order to linearize Planck's function.

Figures 2.1.2 and 2.1.3 show weighting functions, the derivatives of transmittance with respect to a vertical coordinate which is the logarithm of integrated water vapor for the channels sensitive to moisture, and the logarithm of pressure (proportional to integrated oxygen content) for channels in the oxygen band. These weighting functions indicate the atmospheric layers from which the thermal emission measured by each channel originates.

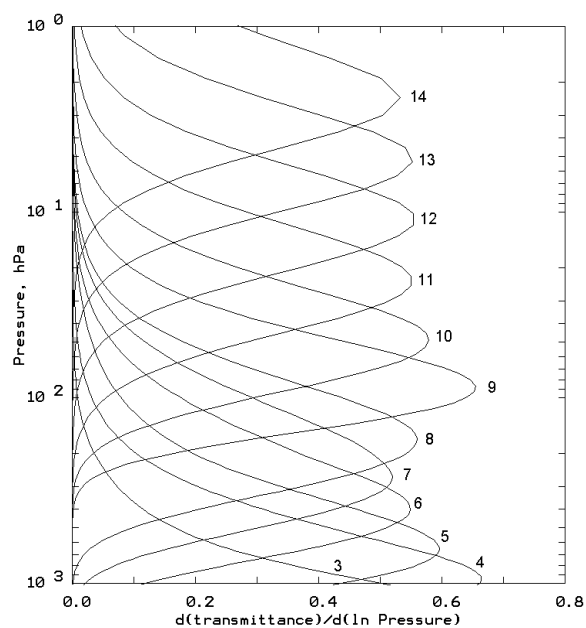


**Figure 2.1.2. Oxygen band weighting functions for unit surface emissivity, with labels showing AMSU channel number.**

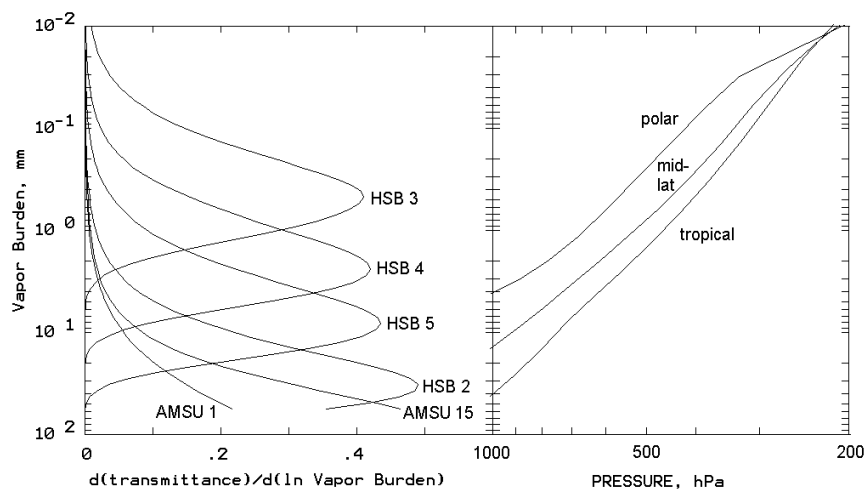


**Figure 2.1.3. Water vapor weighting functions for unit surface emissivity (left) and vapor burden vs. pressure in three different climatologies (right), for the labelled channels.**

The ability of the rapid algorithm to approximate a line-by-line calculation was tested on a set of 300 profiles from the TOVS Initial Guess Retrieval (TIGR) (Chedin, *et al.*, 1985) ensemble. The first 100 profiles from each of the tropical, mid-latitude, and polar groups were used. Figure 2.1.4 shows brightness temperature error estimates (mean  $\pm 1$  standard deviation) at nadir, with surface emissivity = 0.7. For the AMSU channels



that are not opaque (1-5, 15-17, 19 and 20), these estimates depend on surface emissivity. Emissivity  $\varepsilon = 0.7$  is typical of ocean at the highest frequencies, and intermediate between ocean and land at the lowest frequencies. Errors for higher-emissivity land surfaces are smaller than those in Figure 2.1.4. The error estimates for channel 14 include the consequences of the magnetic field approximation. The output files contain a flag structure, `MW_tair_range`, which indicates whether the final temperature at any pressure level  $> 0.1$  hPa lies outside of the range of profiles for which the rapid algorithm has been found to reproduce a line-by-line calculation within the instrument sensitivity. Different bits are set for temperatures outside the validated range by  $<10\%$ , 10 to 25%, or  $>25\%$ .

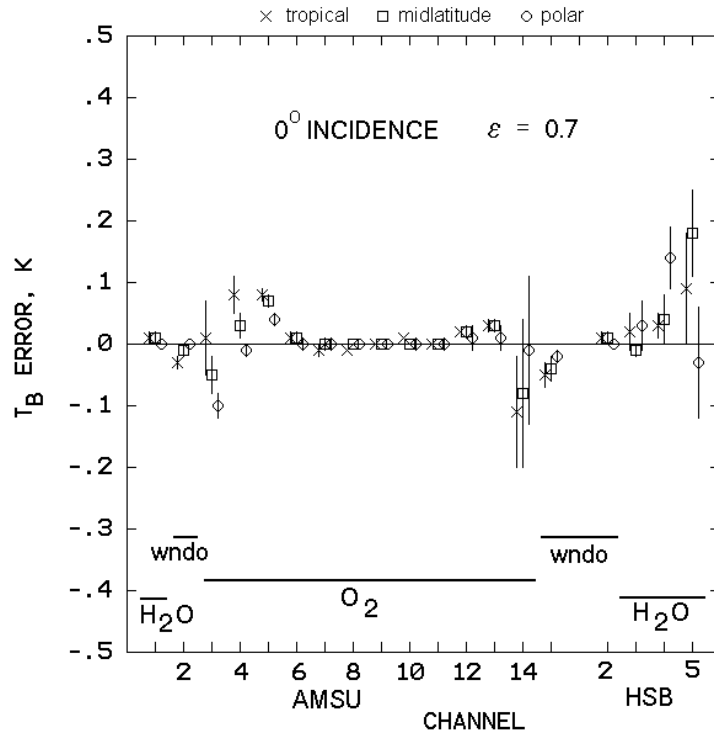


**Figure 2.1.4. Brightness temperature errors (rapid algorithm minus line-by-line algorithm) for AMSU and HSB channels. Vertical lines indicate  $\pm 1$  standard deviation;  $\varepsilon$  is the surface emissivity.**

### 2.1.5. Microwave Surface Brightness Model

The surface brightness temperature spectrum  $\Theta_s$  is modeled by a six-parameter  $(T_0, T_1, T_2, \nu_1, \nu_2, s)$  curve, added to an *a priori* surface brightness

$$\Theta_s(\nu) = \varepsilon_0(\nu) T_{s0} + T_0 + T_1 \nu^s / (\nu^s + \nu_1^s) + T_2 \nu^s / (\nu^s + \nu_2^s) \quad (2.1.7)$$

where  $\varepsilon_0(\nu)$  is a preliminary estimate of emissivity for the surface type obtained from the classification algorithm described in Section 3.5 and 3.6, and  $T_{s0}$  is the *a priori* surface temperature. The parameters  $T_0$ ,  $T_1$ ,  $T_2$  are used in the retrieval solution to adjust the spectrum (they have *a priori* value zero), while  $\nu_1$ ,  $\nu_2$  and  $s$  are assigned according to surface type. The last three terms in Eqn. (2.1.7) also help to correct for effects such as ocean surface roughness, errors in the dielectric constant model, misclassification of the surface, or errors in the estimated land fraction within the footprint.

In Figure 2.1.5, the rapid transmittance algorithm is tested against measurements made by AMSU-A on the NOAA-15 satellite (see Rosenkranz, 2003) and HSB on Aqua (see Rosenkranz and Barnet, 2006). The calculated brightness temperatures are based on coincident radiosonde profiles, using window channels to infer the surface emissivity. Sidelobe corrections from Mo (1999) were applied to the AMSU-A measurements in the figure, but no corrections were made to the HSB measurements.

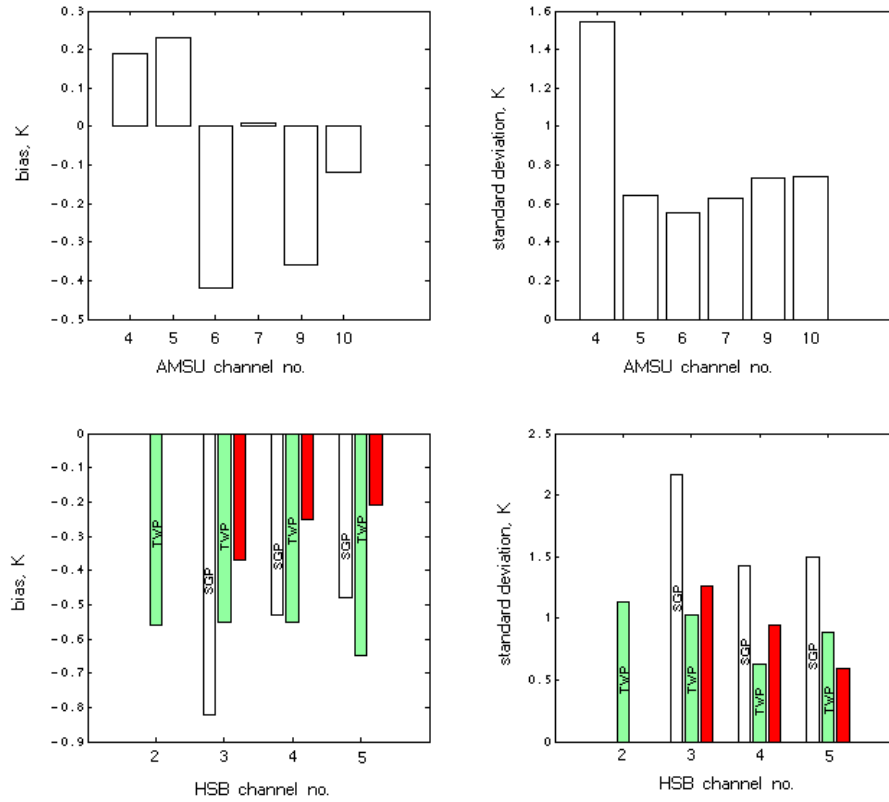


**Figure 2.1.5. Statistics of differences between measured brightness temperatures and brightness temperatures calculated from radiosonde profiles. Three profile ensembles are shown for HSB.**

## 2.2. Radiative Transfer of the Atmosphere in the Infrared

Physical retrievals of atmospheric parameters attempt to minimize differences between computed and observed radiances. The accuracy of the retrieval is therefore directly related to the accuracy of the computed radiances. AIRS observes upwelling monochromatic radiances convolved with the instrument spectral response function (SRF). An exact calculation of the observed radiances therefore requires convolution of simulated monochromatic radiances. These computed radiances are complicated functions of the atmospheric state (temperature, pressure, gas amount), the gas transmittances, and the AIRS SRF. Since the atmospheric emission lines can have widths as small as  $\sim 0.001 \text{ cm}^{-1}$ , the wavenumber grid scale for exact radiance calculations must have a similar spacing. This small grid spacing, combined with the time-consuming SRF convolutions, makes a monochromatic calculation of radiances orders of magnitude too slow for practical use. Instead, we use a fast radiative transfer model that is based on pre-computed convolved atmospheric transmittances for each spectral channel. Then the radiative transfer can be performed on a per-channel basis rather than on a finely spaced monochromatic wavenumber grid.

The starting point for understanding the AIRS radiative transfer algorithm (AIRS-RTA) is the monochromatic radiative transfer equation. The monochromatic radiance leaving the top of a non-scattering atmosphere is

$$R(\nu, \theta) = \epsilon_s(\nu) B(\nu, T_s) \tau(\nu, p_s, \theta) + \int_{p_s}^0 B(\nu, T) \frac{d\tau(\nu, p, \theta)}{dp} dp + \rho_s(\nu) H_{sun}(\nu) \tau(\nu, p_s, \theta) \tau(\nu, p_s, \theta_{sun}) \cos(\theta_{sun}) + R_d \quad (2.2.1)$$

where  $B(\nu, T)$  is the Planck function emission at frequency and temperature  $T$ ,  $\tau(\nu, p, \theta)$  is the transmittance between pressure  $p$  and the satellite at viewing angle  $\theta$  (not brightness temperature, as in the previous section), and  $T_s$ ,  $\epsilon_s$ , and  $\rho_s$  (different from the ratio of secants defined before equation 2.1.5) refer to the Earth's surface temperature, emissivity, and reflectivity respectively. The solar radiance incident at the top of the atmosphere is represented by  $H_{sun}$ , while  $R_d$  is a relatively small radiance contribution arising from the reflection of the downwelling atmospheric thermal emission

$$R_d(\nu) = 2\pi\rho_s\tau(\nu, p_s, \theta) \int_{p=0}^{p_s} B(\nu, T) \int_{\theta_i=0}^{\frac{\pi}{2}} \sin(\theta_i) \cos(\theta_i) \frac{d\tau_d(\nu, p, \theta_i)}{dp} dp d\theta_i \quad (2.2.2)$$

where  $\tau_d$  is the transmittance between pressure  $p$  and the surface. The dependence of temperature and angle on pressure (altitude) has been omitted in the above equations, as well as the dependence of the transmittances on temperature and gas abundance.

The AIRS-RTA allows the integration of the radiative transfer equation in a discrete form over 100 atmospheric layers. For reasons of clarity and brevity we omit further discussion of the last two terms in Equation (2.2.1), except to note that they are included in the AIRS-RTA by simplified approximations. A discrete form of the radiative transfer equation can then be written conveniently as

$$R_{meas} = \int R(\nu) f(\nu - \nu_0) d\nu = \int (\varepsilon_s B(T_s) \tau_N + \sum_{i=1}^N B(T_i) (\tau_{i-1} - \tau_i)) f(\nu - \nu_0) d\nu \quad (2.2.3)$$

where the atmospheric layers are numbered from space to the surface, 1 to  $N$  respectively.  $B(T_i)$  is the Planck emission for layer  $i$  at temperature  $T_i$ ,  $\tau_i$  is the transmittance from layer  $i$  to space, inclusive, and  $f(\nu - \nu_0)$  is the AIRS SRF for the channel centered at  $\nu_0$ . The emissivity and Planck function are nearly constant over the narrow width  $\Delta\nu$  of the AIRS channels, so they may be moved outside the integral. After integrating the transmittances, we are left with the channel-averaged form of the radiative transfer equation,

$$R_{meas} = \varepsilon_s B(T_s) \tau_N + \sum_{i=1}^N B(T_i) (\tau_{i-1} - \tau_i) \quad (2.2.4)$$

where all terms now represent appropriate channel-averaged quantities.

The polychromatic approximation introduced in the above relation replaces the monochromatic layer-to-space transmittances with transmittances convolved with the SRFs. This in effect convolves the outgoing radiances, allowing computation of the radiative transfer at a single frequency per channel. In most cases, the AIRS channel radiances calculated from the above equation using convolved layer-to-space transmittances differ from the convolved monochromatic AIRS channel radiance

brightness temperatures by  $\leq 0.05$  K, assuming perfect layer-to-space convolved transmittances.

Figure 2.2.1 illustrates the large difference in spectral resolution between the upwelling monochromatic radiation and an AIRS brightness temperature spectrum. Because of this large difference in spectral resolution one cannot derive the layer-to-space transmittances directly from the product of the convolved layer transmittances since Beer's law is no longer valid. Overcoming this problem is one of the major issues in the development of a model for fast, parameterized, convolved layer transmittances.

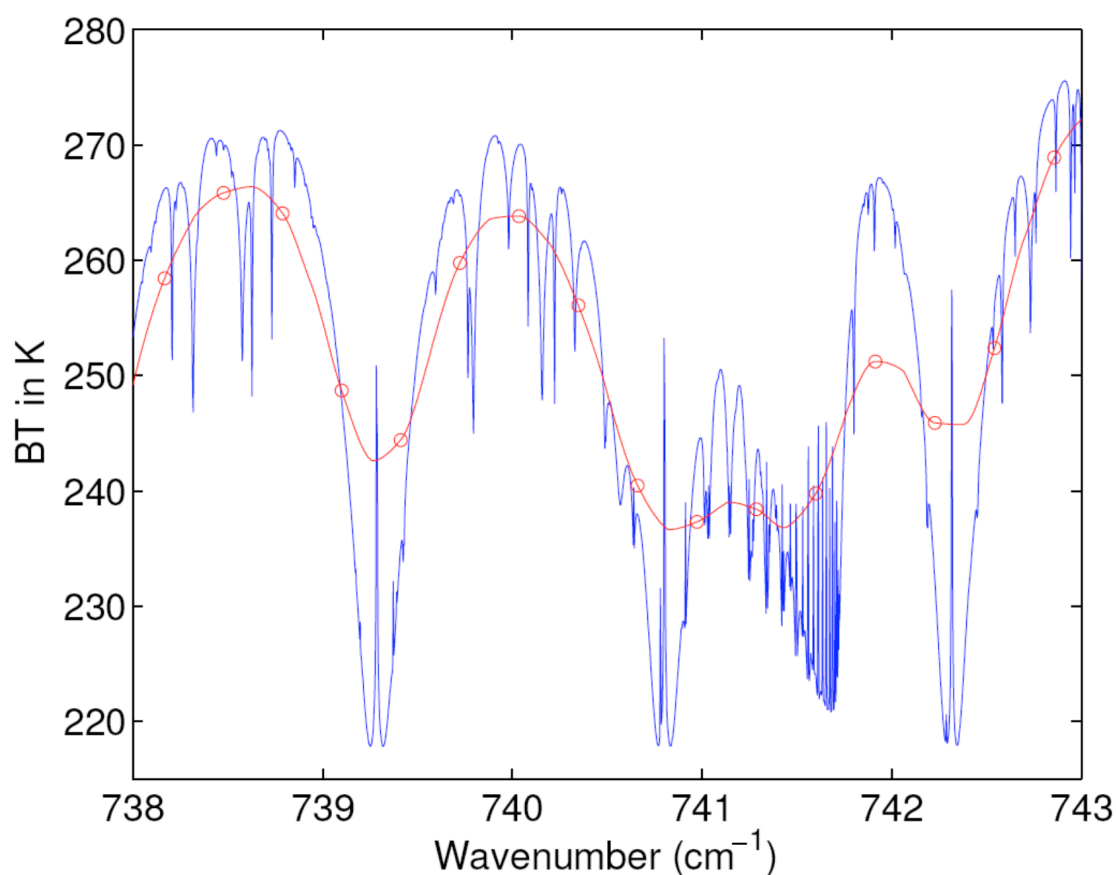


**Figure 2.2.1. Simulated monochromatic (blue) and AIRS SRF convolved (red) brightness temperature spectra. The red circles indicate the actual AIRS channel centroids.**

In the following sections we discuss the major issues in developing the AIRS-RTA, which include: (1) forming a discrete vertical grid for integrating the radiative transfer equation, (2) parameterizing the layer transmittances as a function of the atmospheric state, (3) the spectroscopy needed to compute atmospheric transmittances, (4) the line-by-line algorithm used to generate the monochromatic transmittances (5) the AIRS spectral response functions.

The flowchart shown in Figure 2.2.2 outlines the flow of activities needed to develop the AIRS-RTA, which is discussed in the following text.

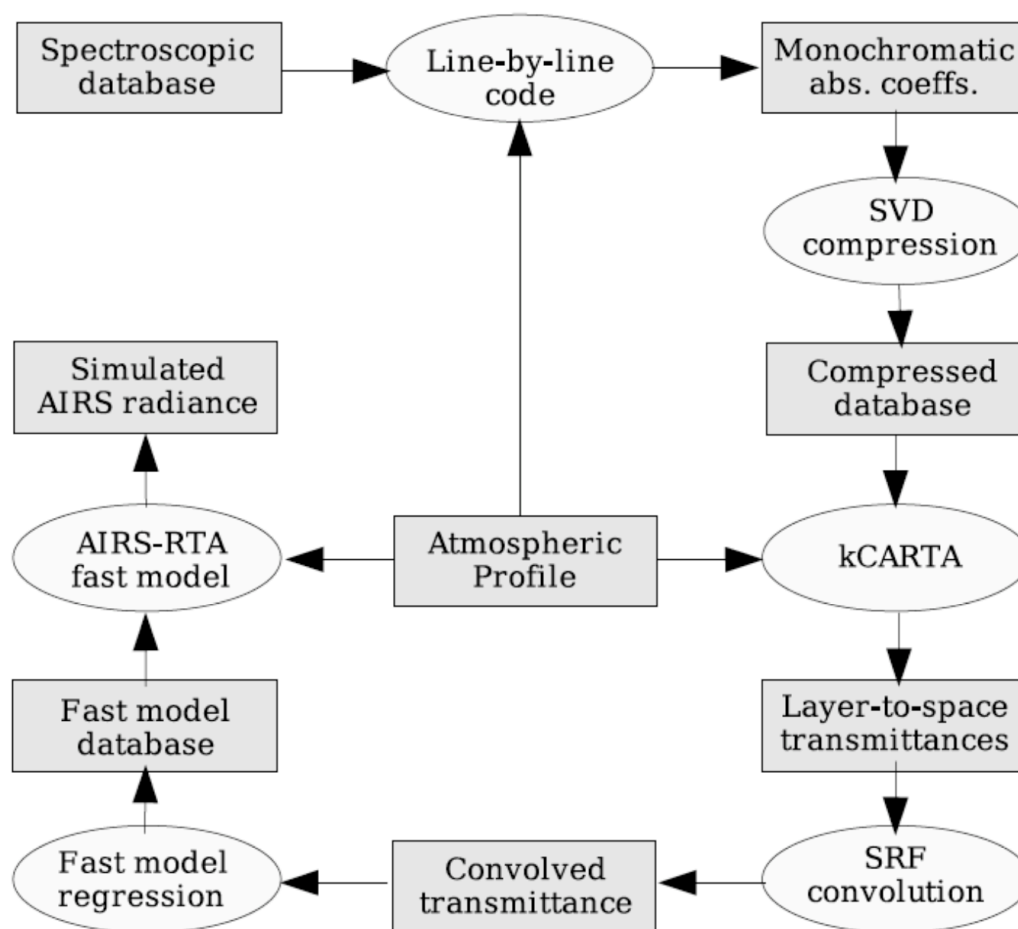


**Figure 2.2.2. Flow diagram for development of the AIRS-RTA.**

### 2.2.1. AIRS Atmospheric Layering Grid

The atmospheric pressure layering grid for the AIRS-RTA model was selected to keep radiative transfer errors below the instrument noise. Grid characteristics are determined by the spectral region(s) of observation, the instrument resolution, and instrument noise. The speed of the final fast transmittance model will depend on the number of layers, so excessive layering should be avoided.

Line-by-line simulations indicate some channels need a top layer with pressures as small as 0.01 hPa (an altitude of  $\sim 80$  km). The region of primary importance to AIRS is the troposphere and lower stratosphere, where layers on the order of 1/3 of the nominal 1-km vertical resolution of AIRS retrievals are desired. Smoothly varying layers facilitate interpolation and avoid large changes in layer effective transmittances. The following relation defines the pressure layer boundaries selected for AIRS

$$P_i = (ai^2 + bi + c)^{7/2} \quad (2.2.5)$$

where  $P$  is the pressure in millibars;  $i$  is the layer boundary index and ranges from 1 to 101; and the parameters  $a$ ,  $b$ , and  $c$  were determined by solving this equation with the following fixed values:  $P_1 = 1100$  hPa,  $P_{38} = 300$  hPa, and  $P_{101} = 0.005$  hPa. The 101 pressure layer boundaries define the 100 AIRS layers. These layers vary smoothly in thickness from several tenths of a kilometer near the surface to several kilometers at the highest altitudes. Figure 2.2.3 shows the layer mean pressure for the 100 AIRS layers.

### 2.2.2. Fast Transmittance Modeling

A number of fast transmittance models have been developed for satellite instruments. However, some of these models have been applied only to the microwave region where the measured radiances are essentially monochromatic and easier to model than the infrared. AIRS required a major new effort in the development of its RTA. Details of our model can be found in Strow, *et al.*, (2003).

The AIRS-RTA most closely follows Susskind, *et al.*, (1983) by parameterizing the optical depths rather than transmittances for channels where the influence of water vapor is small. Channels sensitive to water vapor are modeled using a variant of the Optical Path

TRANsmittance (OPTRAN) algorithm developed by McMillin, *et al.*, (1979, 1995). The AIRS infrared fast model is thus a hybrid of Susskind's approach and OPTRAN.

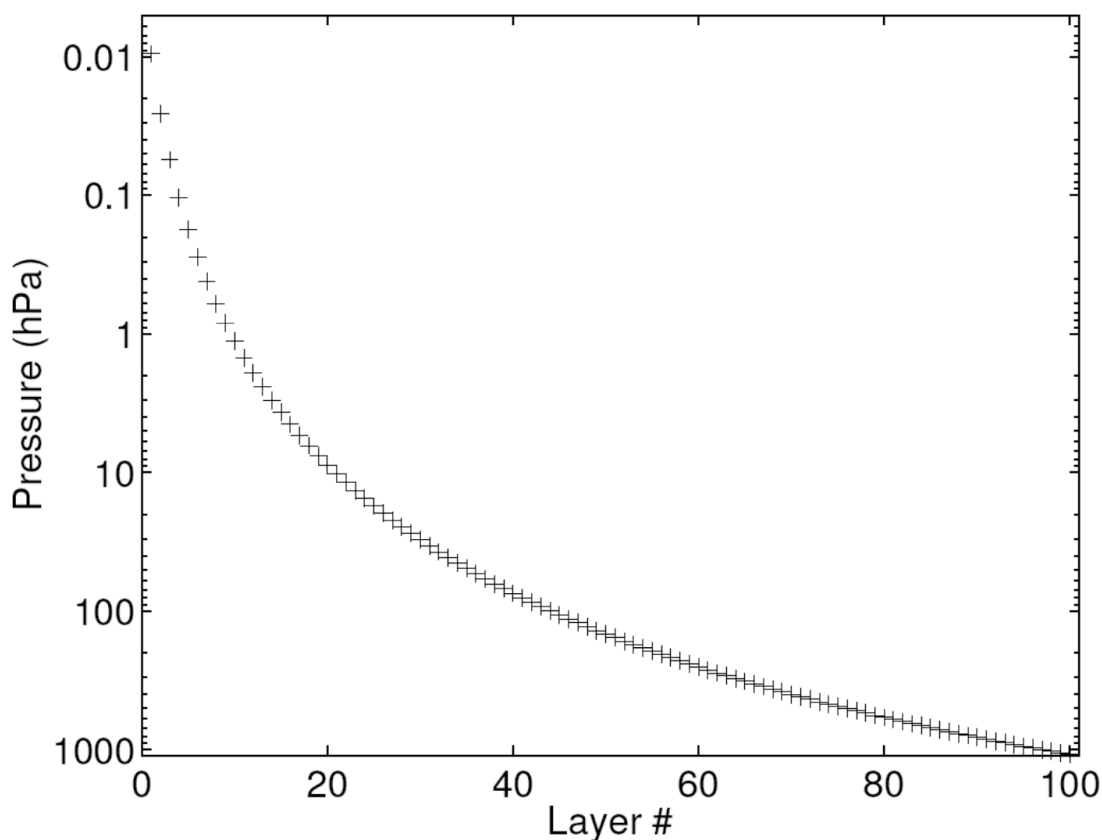


**Figure 2.2.3. Mean pressure of the AIRS-RTA 100 layers.**

Following Susskind *et al.*, the AIRS-RTA model produces equivalent channel averaged optical depths,  $k$ , which are related to the layer transmittances,  $\tau$ , by  $\tau = \exp(-k)$ . The optical depth is the product of the absorption coefficient and the optical path. For AIRS wavelengths, a fast model for  $k$  is much more accurate than a model that directly returns layer  $\tau$ . Optical depth  $k$  is computed for each of the 100 atmospheric layers used for AIRS radiative transfer. The current AIRS-RTA model allows temperature and local scan angle to vary, along with amounts of water vapor, ozone, methane, carbon monoxide and carbon dioxide. All other gases are treated as “fixed” in that we only parameterize their dependence on temperature, not amount. So, although the observed radiances are primarily



sensitive to temperature via the Planck function, the temperature dependence of the calculated transmittances is also important.

The following discussion describes the parameterization of the convolved layer transmittances as a function of the atmospheric state. Most of the complications of this parameterization arise from the inapplicability of Beer’s law, necessitating terms in the transmittance parameterization for a given layer that depend on layers above. These parameterizations, which are functions of the atmospheric profile, are derived from least-squares fits to a widely varying set of 48 atmospheric profiles to ensure that we can faithfully produce the appropriate transmittances under a wide range atmospheric conditions. We call this set of profiles our “regression profiles”.

### ***Breakout of Radiance Contribution by Gases***

Once the atmospheric layering grid and regression profiles (see later discussion) are selected, the monochromatic layer-to-space transmittance can be calculated. The gases are distributed into sub-groups that are either fixed or variable. The details of how the transmittance model simultaneously handles several variable gases is somewhat complicated and beyond the scope of this document (Strow et al, 2003). For simplicity, this discussion is restricted to the fixed gases ( $F$ ), water vapor ( $W$ ), and ozone ( $O$ ). The contributions by the other variable gases are similar to those of  $W$  and  $O$ . The monochromatic layer-to-space transmittances for the 48 regression profiles are calculated for each pressure layer, grouped into the following three sets, and convolved with the AIRS SRF

$$\begin{aligned} F_l &= \tau_l(\text{fixed}) \\ FO_l &= \tau_l(\text{fixed} + \text{ozone}) \\ FOW_l &= \tau_l(\text{fixed} + \text{ozone} + \text{water}) \end{aligned} \tag{2.2.6}$$

Water continuum absorption is excluded since it varies slowly with wavenumber so does not need to be convolved with the AIRS SRF. In addition, separating the water continuum improves our fit of the local line water transmittance. Later, the water continuum is factored into the total transmittance as a separate term.

For each layer  $l$ , the convolved layer-to-space transmittances are ratioed with transmittances in the layer above,  $l - 1$ , to form effective layer transmittances for fixed  $F$ ,  $W$ , and  $O$  as

$$\begin{aligned} F_l^{eff} &= \frac{F_l}{F_{l-1}} \\ O_l^{eff} &= \frac{FO_l}{FO_{l-1}} \div \frac{F_l}{F_{l-1}} \\ W_l^{eff} &= \frac{FOW_l}{FOW_{l-1}} \div \frac{FO_l}{FO_{l-1}} \end{aligned} \quad (2.2.7)$$

Forming these ratios in the above manner reduce the errors inherent in separating the gas transmittances after the convolution with the instrument spectral response function. The total effective layer transmittance can be recovered as

$$FOW_l^{eff} = F_l^{eff} \times O_l^{eff} \times W_l^{eff} = \frac{FOW_l}{FOW_{l-1}} \quad (2.2.8)$$

The convolution of a product of terms is in general not the same as the product of the terms convolved individually. However, the above formulation guarantees the product of all the layer transmittances from layer  $l$  to  $N$  gives exact  $FOW_l$  if the layer transmittances are exact.

The zeroth layer transmittance (i.e., when  $l - 1 = 0$ ) is taken to be exactly 1.0, representing space between the spacecraft and the atmosphere. The negative logarithm of these layer effective transmittances is taken to get effective layer optical depths

$$\begin{aligned} k_{fixed} &= -\ln(F^{eff}) \\ k_{ozone} &= -\ln(O^{eff}) \\ k_{water} &= -\ln(W^{eff}) \end{aligned} \quad (2.2.9)$$

which become the dependent variables in the fast model regression.

### **Predictors**

The independent variables in the fast model regression, called the predictors, are quantities relating to the atmospheric profile. (Example predictors are given below.) The optimal set of predictors used to parameterize the effective layer optical depth depends

upon the gas, the instrument SRFs, the range of viewing angles, the spectral region, and even the layer thicknesses. In short, no one set of predictors is likely to work well in every case. Finding the set of predictors which give the best results is, in part, a matter of trial and error. However, there are some general trends.

For an instrument such as AIRS with thousands of channels, it is difficult to develop optimal predictors for each channel. The AIRS-RTA uses seven sets of predictors, each corresponding to a subset of channels. These sets of predictors were determined by extensive trial and error testing, as well as consideration of the relative importance of the variable gases in each channel. Supplemental sets of predictors are used for OPTRAN water vapor, the water vapor continuum, and variable CO<sub>2</sub>.

The regression algorithm is prone to numerical instabilities if the predictors vary too greatly. Consequently, we define the predictors with respect to the values of a reference profile, either by taking a ratio or an offset. There is also a danger of numerical instability in the regression from interactions of some of the predictors. Sensitivity of the output to small perturbations in the predictors is avoided by systematic testing, but there are practical difficulties in detecting small problems since we are performing on the order of one million regressions.

As an example, the predictors for the fixed gases for one of the eight sets are

$$1) a \quad 2) a^2 \quad 3) aT_r \quad 4) aT_r^2 \quad 5) T_r \quad 6) T_r^2 \quad 7) aT_z \quad 8) aT_z/T_r \quad (2.2.10)$$

where  $a$  is the secant of the local path angle,  $T_r$  is the temperature ratio  $T_{profile}/T_{reference}$ , and  $T_z$  is the pressure weighted temperature ratio above the layer

$$T_z(l) = \sum_{i=2}^l P(i)P(i) - P(i-1)T_r(i-1) \quad (2.2.11)$$

where  $P(i)$  is the average layer pressure for layer  $i$ . The predictors for the variable gases can involve more complicated dependencies on the gas and the pressure-weighted gas ratios above the layer, similar to the temperature term defined above. Note that terms like  $T_z$  (or  $W_z$ , etc. for the variable gases) make the layer  $l$  transmittance dependent on the temperature (or gas amounts) in the layers above  $l$ .

### ***Regressions for Fast Transmittance Parameters***

The accuracy of radiative transfer calculations with the AIRS-RTA model is improved significantly by weighting the variables prior to performing the regression. Radiative transfer is insensitive to layers for which the change in layer-to-space transmittance across the layer is approximately zero. This occurs when either the layer effective transmittance is approximately unity, or the layer-to-space transmittance is approximately zero. Therefore, the data going into the regression are not all of equal importance to the final accuracy of radiative transfer calculations made with the model. We found it useful to weight the data in terms of both effective layer optical depth as well as the total optical depth of all the layers above the layer under consideration.

The spectral dependence of the fitting errors is shown in Figure 2.2.4 and a histogram of these error estimates in Figure 2.2.5. The errors are calculated with respect to the regression profile set, comparing the RMS difference between the brightness temperatures of input data and the AIRS-RTA model calculated values. These graphs include errors from all six angles used for regression profiles. They do not include errors associated with the parameterization of the reflected thermal and reflected solar radiation.

During the development of the AIRS-RTA, the RMS error estimates were computed for a large independent set of profiles. The RMS differences for the independent profiles were generally similar to those for the regression profiles. The regression profiles represent a wide range of possible conditions, with a number of extreme cases. It is important to recognize, however, that the AIRS-RTA solutions vary depending upon the selection of regression profiles.

### ***Regression Profiles***

One other necessary pre-processing step is the selection of a set of profiles for calculation of the layer-to-space transmittances. The transmittances for these profiles become the regression data for the fast transmittance coefficients. These profiles should span the range of atmospheric variation but should be weighted towards the more typical cases. The range of variation provides the regression with data points covering the range of possible atmospheric behavior, while the weighting of the mix of profiles towards more typical cases produces a transmittance model that works best on more common cases.

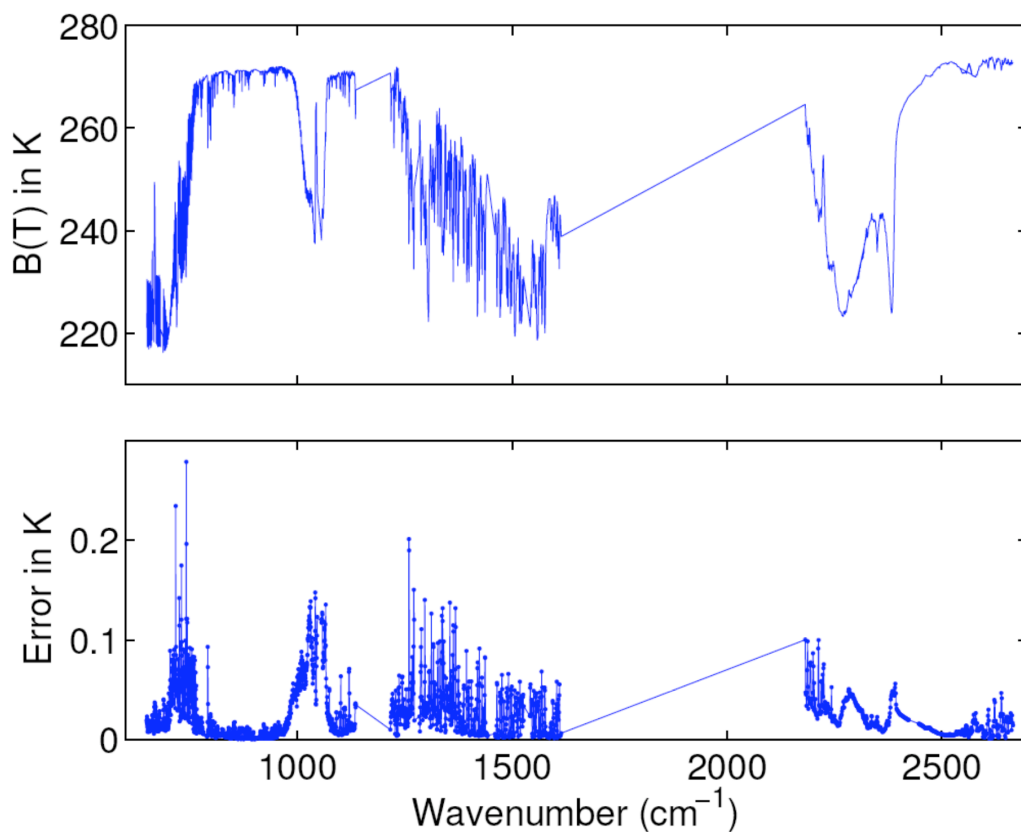


Figure 2.2.4. RMS error estimates of the AIRS-RTA model.

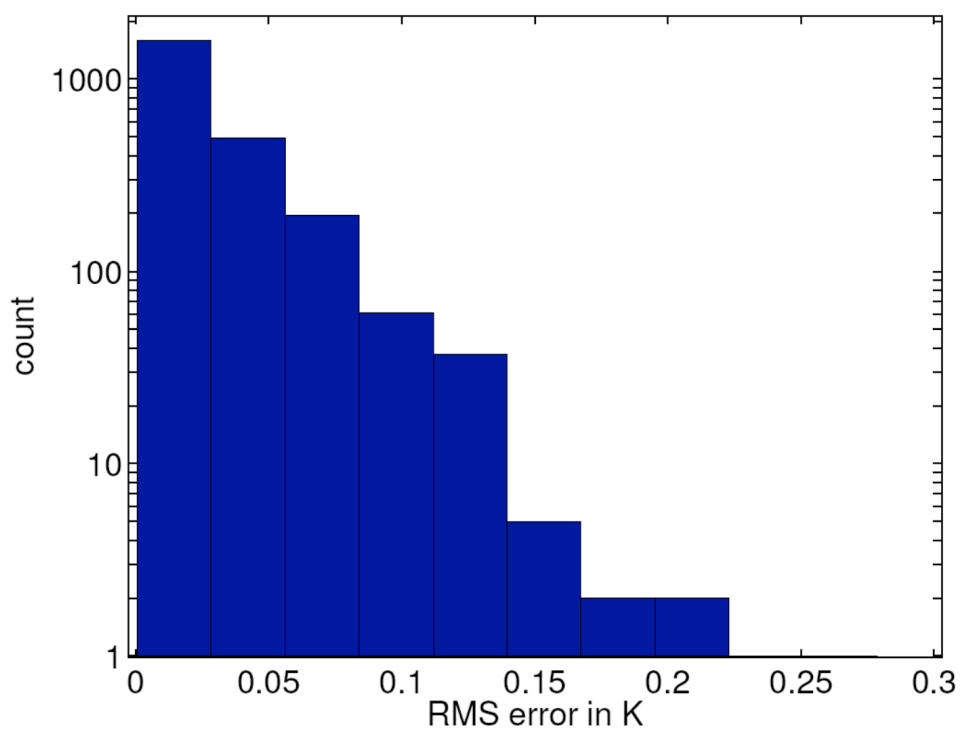


Figure 2.2.5. Histogram of the AIRS-RTA model fitting errors for all channels.

The process of calculating and convolving monochromatic layer-to-space transmittances is generally computationally intensive, thus imposing a practical limit on the number of profiles one can calculate for use in the regression. As discussed earlier, 48 regression profiles (at 6 viewing angles each) are sufficient to cover most atmospheric behavior. This number is a compromise between the available time and computing resources and the need to include a wide range of profile behavior in the regression. Choosing too few profiles leads to accuracy problems for profiles outside the range of behaviors considered. Choosing more profiles than necessary does not negatively affect the fast model, but does consume extra time and computer resources.

Each profile in the regression set should cover the necessary pressure (altitude) range with data for temperature as well as absorber amount for each of the gases allowed to vary. The fixed gases include all whose spatial and temporal concentration variations have a negligible impact on the observed radiances. As previously mentioned, the variable gases are H<sub>2</sub>O, O<sub>3</sub>, CO, CH<sub>4</sub>, and CO<sub>2</sub>. All other gases are included in the “fixed gases.” CO<sub>2</sub> is handled differently than the other variable gases, and only two CO<sub>2</sub> absorber amount profiles are used: a standard amount profile and a perturbed amount profile. The standard amount CO<sub>2</sub> profile is treated as a fixed gas. A very simple and accurate parameterization is used to model the difference in transmittance between the standard CO<sub>2</sub> profile transmittances and the perturbed CO<sub>2</sub> profile transmittances (Strow et al., 2003).

For those satellite-viewing angles relevant to the AIRS instrument (0 to 49 degrees), the effects of viewing angle can be approximated fairly well by multiplying the nadir optical depth by the secant of the local path angle. This approximation neglects the minor refractive effect at large angles. Due to the curvature of the Earth, the local path angle is in general not the same as the satellite viewing angle, but is related to it by a fairly simple equation. Local atmospheric path angles of 0, 32, 45, 53, 60, and 63 degrees are used in the regression profiles to cover the 0-49 degree satellite view angle range. An additional six angles between 69 and 84 degrees are used for the shortwave channels where transmittances at large angles are needed to model the reflected solar radiance.

### 2.2.3. Spectroscopy

The ultimate goal of AIRS-RTA development is AIRS computed radiances without significant errors. This requires a fast model that can compute accurate transmittances. Even if the fast model RMS fitting errors are small, the accuracy of the transmittances are dependent upon the quality of the spectroscopic line parameters and line-shape models used to compute the monochromatic transmittances.

Due to the dominance of either CO<sub>2</sub> or H<sub>2</sub>O absorption in the majority of AIRS channels, the most important spectroscopy errors are those in the line parameters and line shapes of these two gases. The line parameters most likely to introduce spectroscopy errors into the fast forward model for AIRS are the line strengths, line widths, and the temperature dependence of the line widths. However, errors in spectral line shapes and continuum absorption are generally more troublesome than line parameter errors.

Currently, the HITRAN-2000 (Rothman, *et al.*, 2003) database is used for most atmospheric line parameters. As so many bands and molecules contribute to the observed radiances, the accuracy of existing line parameters is difficult to assess. Based upon our analysis of AIRS observations and calculated radiances, we estimate the combined effects of line parameter and line-shape model errors in the computed optical depth of the stronger absorbing “fixed” gases (which in most spectral regions are dominated by CO<sub>2</sub>) are typically about 5%, while for water vapor the optical depth errors are about 10%.

Errors in the spectral line shapes of CO<sub>2</sub> and H<sub>2</sub>O are much more problematic than line parameter errors. Because of the large optical depths of CO<sub>2</sub> and H<sub>2</sub>O in the atmosphere, their spectral line wings can be important, especially for remote sensing of temperature and humidity. For example, AIRS channels with the sharpest weighting functions are located between lines or in the line wings, where knowledge of the spectral line shape is most important. Moreover, accurate measurements of the line wing absorption are exceedingly difficult due to problems simulating atmospheric optical depths in a laboratory cell, especially for H<sub>2</sub>O. It is also tedious and expensive to make these large optical depth measurements at the low temperatures found in the upper troposphere.

Figure 2.2.6 shows the optical depth “tuning” used with the Version 4 and later AIRS-RTA processing. These multipliers are used to scale the indicated component of the

optical depth inside the AIRS-RTA. These are empirically determined values, and some small portion of these adjustment may be due to error sources other than spectroscopy. Tracing these adjustments back to line parameter errors is no simple task and has not yet been attempted.

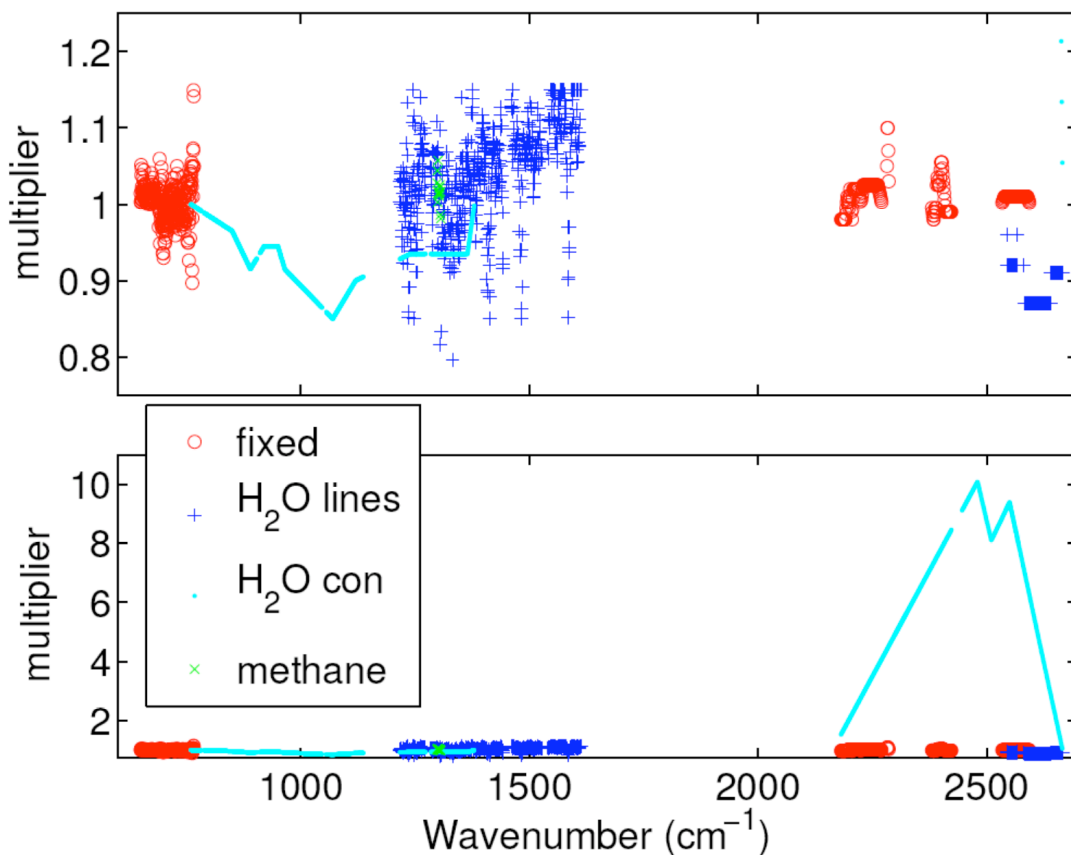


**Figure 2.2.6. Optical depth tuning used in the Version 4 and later AIRS-RTA. The bottom panel shows the same data as the top panel, but with the vertical range expanded to illustrate the large adjustment to the water continuum in the shortwave channels.**

Figure 2.2.7 shows the effects of our optical depth tuning on AIRS radiances. The data set consists of the clearest night-time AIRS observations matched with sondes launched as part of the AIRS validation campaign. The sonde profiles were used with the AIRS-RTA to compute simulated radiances, which were then differenced with the observations. The sonde observations did not extend to the stratosphere, so the bias in the  $15\text{-}\mu\text{m}$  and  $4.3\text{-}\mu\text{m}$  stratospheric channels should be ignored. We solved for an effective



surface skin temperature using the AIRS super-window channel at  $2616\text{ cm}^{-1}$ , so the bias there has been forced to zero.

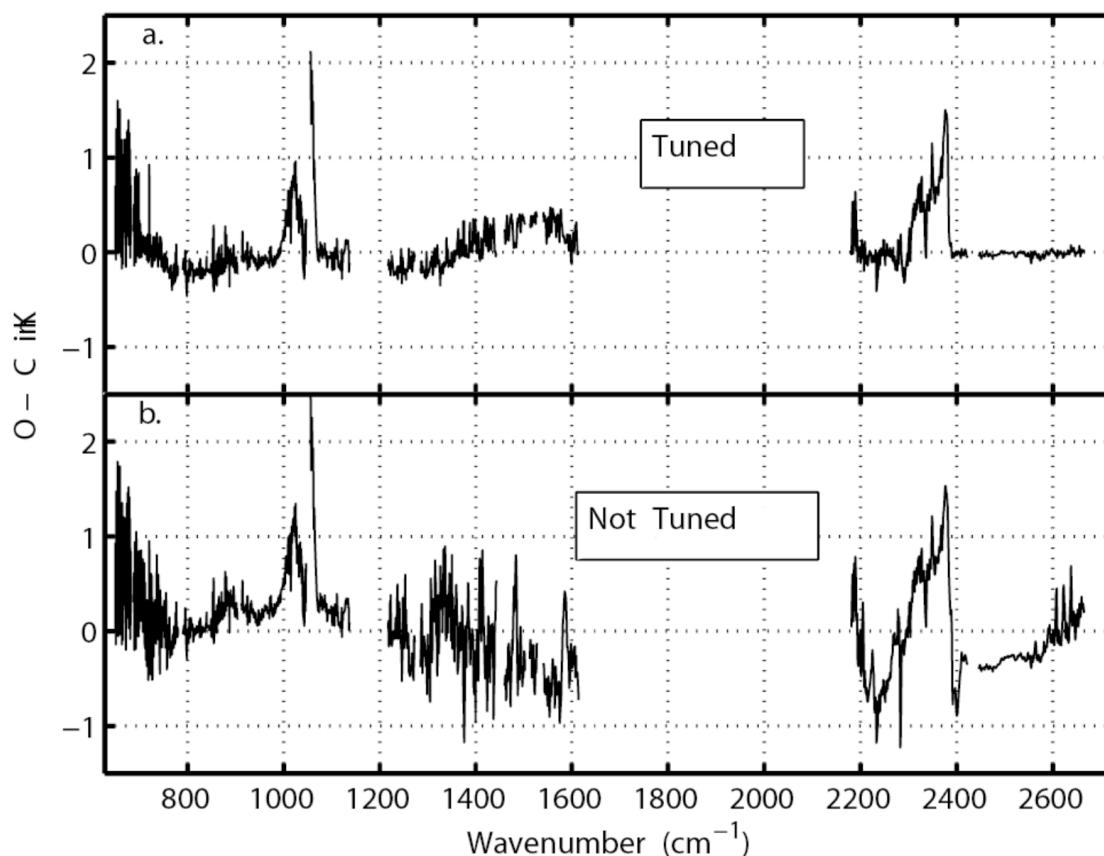


**Figure 2.2.7. Comparison of observed - calculated brightness temperatures with and without optical depth tuning.**

#### *2.2.4. Monochromatic Transmittance Calculations*

The monochromatic layer-to-space transmittances used to determine the parameters of the AIRS-RTA model are indirectly generated using our custom line-by-line code (UMBC-LBL). Building a custom LBL code allowed us to incorporate those features we deemed desirable, including our Q-, P-, and R-branch  $\text{CO}_2$  line-mixing model which has a significant effect on the optical depths in the  $15\text{-}\mu\text{m}$  and  $4\text{-}\mu\text{m}$  regions.

Currently, 48 profiles are used in the regressions for the fast transmittance parameters. Because line-by-line (and especially Q/P/R branch line mixing) calculations are very slow, we developed a new pseudo line-by-line algorithm called the kCompressed Atmospheric Radiative Transfer Algorithm (kCARTA) to allow the (relatively) fast

computation of nearly monochromatic transmittances and radiances. The UMBC-LBL was used to compute a very large look-up table of monochromatic layer optical depths for a set of 11 reference atmospheric profiles. To compute the optical depths for the desired profile, the kCARTA program interpolates the lookup table optical depths for temperature and scales for absorber amount. Any change in the physics of the line-by-line code or line parameter database requires a recalculation of the affected portion of the look-up table.

The kCARTA database consists of many individual look-up tables each covering a  $25\text{-cm}^{-1}$  interval with 10,000 points ( $0.0025\text{-cm}^{-1}$  spacing) for 100 pressure layers (0.009492 to 1085 hPa) and 11 temperature profiles. The temperature profiles are the U.S. Standard profile, and 10 profiles offset from it in  $\pm 10$  K increments. On average, 7 gases must be included per  $25\text{-cm}^{-1}$  region. The continua due to gases such as  $\text{N}_2$  and  $\text{O}_2$  are also included in these tables. Optical depths are computed using a  $0.0005\text{ cm}^{-1}$  grid and then averaged to the database grid spacing of  $0.0025\text{ cm}^{-1}$ .

Consequently, the highest altitude optical depths are not truly monochromatic, but exhibit good integrated optical depths. The relatively large width of the AIRS Spectral Response Function (SRF) results in negligible errors due to this averaging.

This large look-up table has been compressed using a Singular Value Decomposition (SVD) method with approximately 50-fold compression. This compression is lossy, but the accuracy of the transmittances remains very high. kCARTA bridges the gap between slow but accurate line-by-line codes, and fast but special-purpose fast transmittance codes. kCARTA is used to calculate the 48 profile transmittances we use as regression data for the AIRS fast transmittance model. The computation time for these transmittances is not a significant fraction of the time involved in creation of a new fast transmittance model. However, the transmittance data files are very large, and the convolution of these monochromatic transmittances with the AIRS SRFs is a time consuming process.

### 2.2.5. *Spectral Response Function Measurements and Modeling*

Inaccuracies in the AIRS spectral response function directly impact the accuracy of the AIRS-RTA, and consequently the accuracy of the AIRS retrieved products. Complete knowledge of the AIRS SRFs derived solely from ground calibration is not possible for two reasons; (1) small changes in the alignment of the AIRS spectrometer/focal plane since launch have shifted the centroids of the AIRS SRFs, and (2) the spectral location of fringes produced by the AIRS entrance aperture filters are dependent on the thermal environment of AIRS in orbit. Both of these effects are relatively small, but our requirements on SRF knowledge are quite stringent.

Since becoming operational in late August 2002, the AIRS channel centroids have remained stable to within 1% of a channel Full Width at Half Maximum (FWHM). An extreme solar flare event in late October 2003 led mission control to shut off the AIRS coolers temporarily. After AIRS was switched back on in early November 2003, it required a few weeks to cool down, and then be re-calibrated back to approximately the same configuration as before the shutdown. While it was possible to adjust the channels to their pre-shutdown centroids, this required a small change to the operating temperature, which resulted in a small relative shift of the fringes. The effects of this shift are small enough to ignore for retrieval purposes, but may need to be accounted for when looking at radiance biases for climate purposes.

Figure 2.2.8 shows the estimated change to the AIRS observed brightness temperatures due to the change in fringe position in November 2003. The effects are negligible in most channels, but not all. The largest change is in the 2200-cm<sup>-1</sup> range which affects the CO sounding channels. The inset plot shows a blowup of this range, and the good agreement between the model and observed change is evidence the fringe and SRF models are fairly accurate.

While we cannot measure the SRFs in orbit, we can measure the channel centroids to fairly high accuracy. Careful analysis of AIRS data indicates the channel centroids drift back and forth by 0.5% of a FWHM (peak-to-peak) over each orbit. The exact reason for this drift is uncertain, but it is probably related to solar heating effects. There is also a long-term drift, with the channels having drifted 0.3% of a FWHM in the first two years since

launch. This slow drift appears to be slowing, and it may not be necessary to take action to maintain the current channel centroids. If it is eventually deemed necessary, it should be possible to again “dial in” the original channel centroids by adjusting the temperature of the focal plane, but this would again cause another relative shift in the fringe positions.

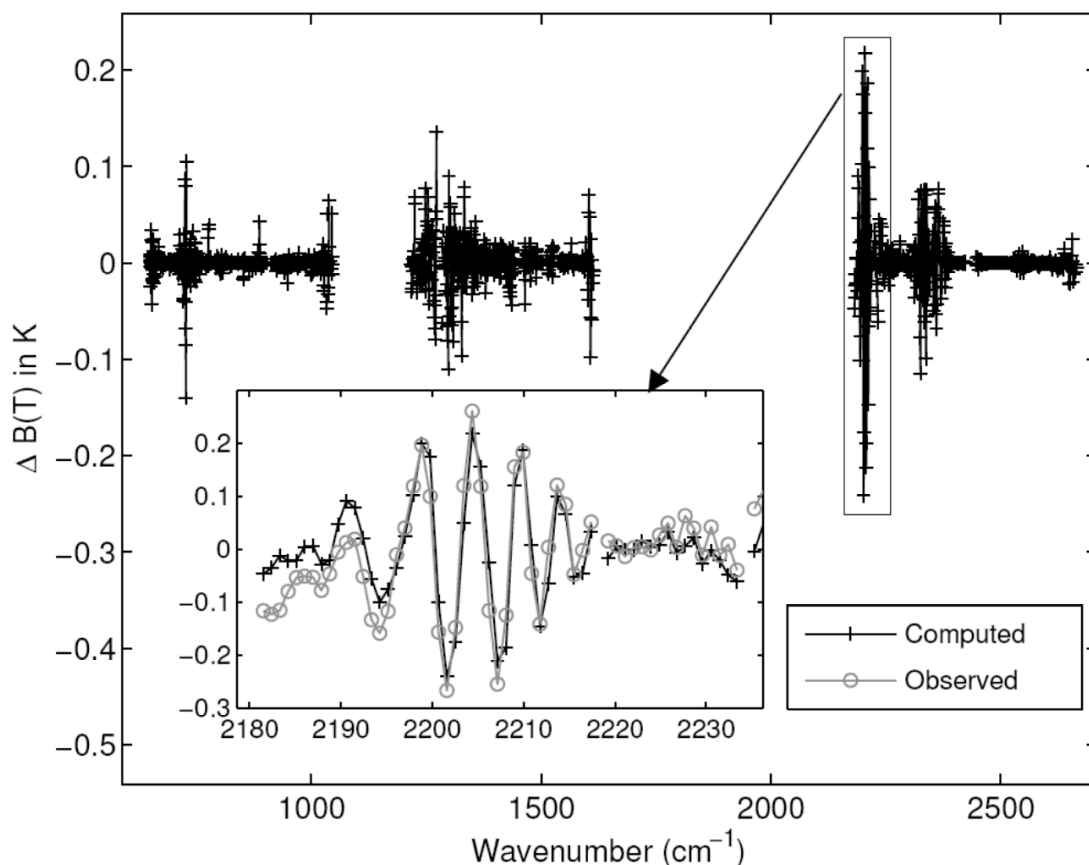


**Figure 2.2.8. Estimated change to AIRS observed brightness temperatures due to the offset in fringe position in November 2003.**

Figure 2.2.9 shows the drift in the AIRS channel centroids as a function of time as well as latitude during the ascending (day-time) portion of Aqua’s orbit. The back-and-forth shift of the centroids with each orbit shows up in this plot as the latitude dependence of the shift. The data used for this plot does not extend to high latitudes, so the full range of the shift with latitude is not shown. The Version 4 and earlier AIRS-RTA and Level 1B data did not account for this small orbital and long-term centroid drift. The effects of a 0.5% error in the channel centroids is shown in Figure 2.2.10. It is possible to apply an

approximate correction for a small centroid error by interpolating the forward model radiances, but that requires knowledge of the centroid position.

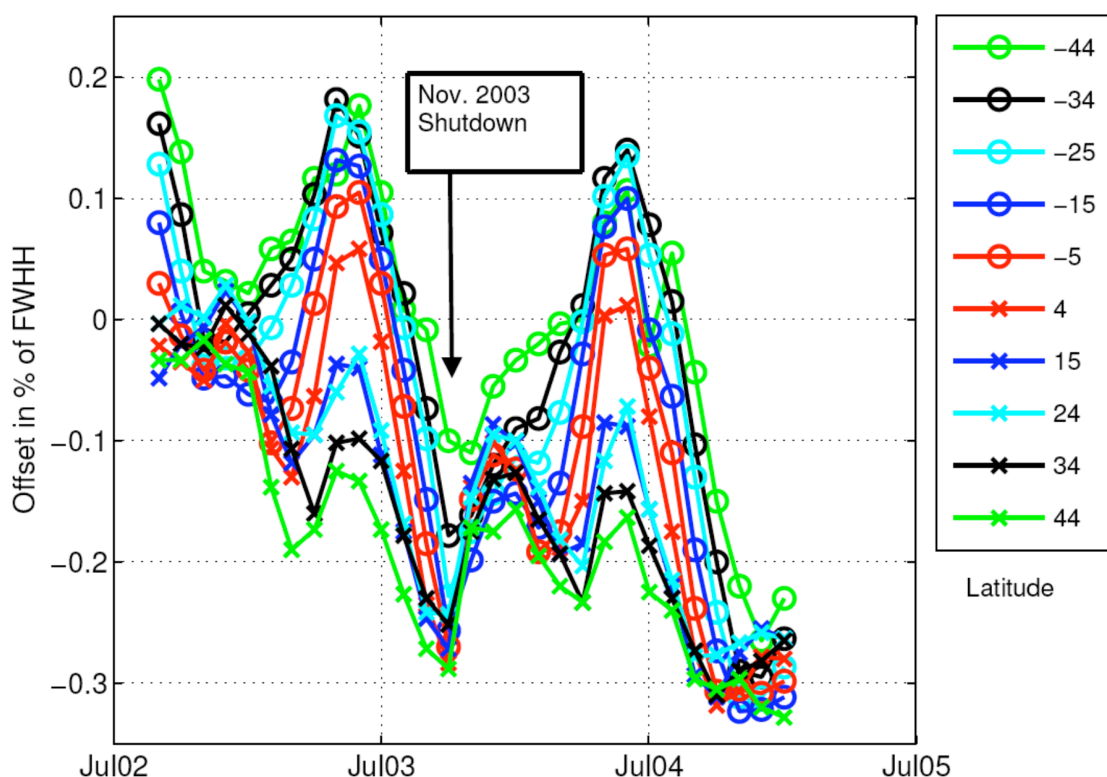


**Figure 2.2.9. Centroid drift versus time and latitude, for ascending (day) orbits.**

### 2.2.6 AIRS-RTA Error Analysis

Table 2.2.1 contains rough estimates of the errors in the AIRS-RTA in units of brightness temperature. They are separated into radiative transfer/spectroscopy errors and SRF knowledge errors. In many cases these errors will be correlated, sometimes of opposite sign. Consequently it is very difficult to properly combine the errors in Table 2.2.1 into a single AIRS-RTA error budget. In addition, most of these errors are highly channel dependent. They have been estimated conservatively and represent upper bounds.

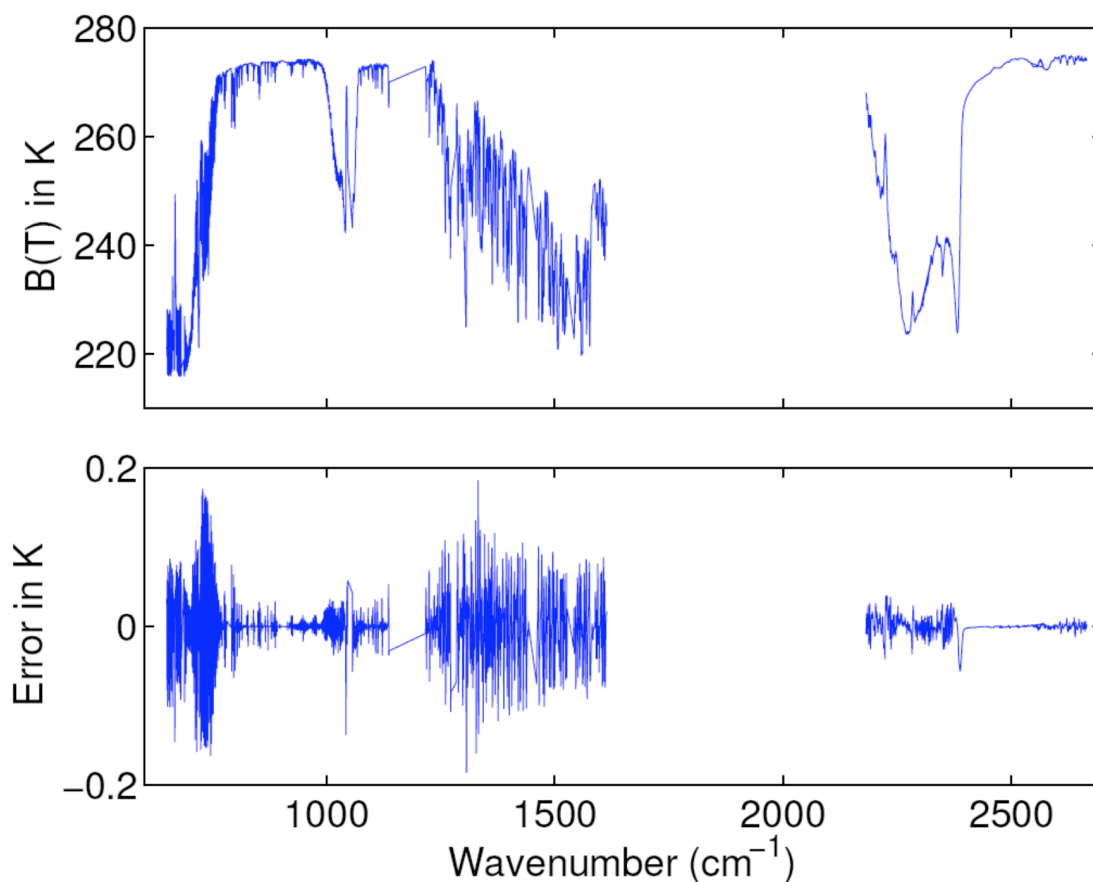


Figure 2.2.10. Brightness temperature error for a 0.5% error in channel centroids.

<b>Radiative Errors</b>	<b>Error (K)</b>	<b>Comment</b>
Fast model fit	0.05 - 0.3	Can be larger for individual profiles
Spectroscopy	0.2 - 0.6	Errors are more likely for water
Reflected thermal	0.0 - 0.2	Proportional to reflectivity
Solar	0.0 - 0.1	Can be much larger if $\rho$ is off
Layering	0.05	Most channel have lower errors
Polychromatic approximation	0.05	Most channel have lower errors
Aerosols	0.0 - 1	Dust can make it through cloud clearing
<b>SRF Errors</b>		
Centroids	0.0 - 0.1	Possible to corrected for
Widths	0.0 - 0.2	Negligible for most channels
Fringes	0.0 - 0.2	Negligible for most channels
Wings	0.0 - 0.2	Negligible for most channels

Table 2.2.1. AIRS-RTA Error Estimates

### 3. RETRIEVAL METHODOLOGY

#### 3.1 Steps in the Retrieval Methodologies Used in Version 6 and 7.

The major steps in the physical retrieval process are as follows:

- (1) A start-up neural net procedure provides an initial solution  $X_0$ .
- (2) Initial clear column radiances  $\hat{R}_{0,i}$  is generated for all  $i$  channels using the initial cloud-clearing coefficients, which were generated based on observed radiances in an ensemble of cloud-clearing channels along with the initial state  $X_0$ .
- (3) A subsequent physical retrieval procedure is performed, starting with the initial guess  $X_0$ , in which AIRS/AMSU observations were used to retrieve (a) surface skin temperature  $T_s$ , surface spectral emissivity  $\varepsilon_v$ , and spectral surface bidirectional reflectance of solar radiation  $\rho_v$ ; (b) atmospheric temperature profile  $T(p)$ ; (c) atmospheric moisture profile  $q(p)$ ; (d) atmospheric ozone profile  $O_3(p)$ ; (e) atmospheric CO profile  $CO(p)$ ; (f) atmospheric CH<sub>4</sub> profile  $CH_4(p)$ ; and (g) retrieve cloud properties and compute  $OLR$ .

These steps are done sequentially, solving only for the variables to be determined in each retrieval step while using previously determined variables as fixed with an appropriate uncertainty attached to them, which was accounted for in the channel noise covariance matrix used in that step (2). The objective in each step in (3) [(a) to (f)] is to find solutions for which computed radiances best match  $\hat{R}_i$  for the subset of channels selected for use in that step, bearing in mind the channel noise covariance matrix. Steps (a) to (f) are ordered to allow for selection of channels in each step that are primarily sensitive to variables to be determined in that step, or in a previous step, and are relatively insensitive to other parameters.

Separation of the retrieval in this manner allows for the solution in each step to be made as linear as possible. Step (g) is performed after the surface and atmospheric conditions have been determined using a selected set of observed radiances  $R_i$ , rather than clear column radiances  $\hat{R}_i$  as used in the other physical retrieval steps.

### 3.2 Channels Used in the Retrieval Steps

Figure 3.2.1 shows a typical AIRS cloud free brightness temperature spectrum and includes the channels used in Version-6 and Version-6 AO for cloud clearing, as well as in each of the different steps of the AIRS physical retrieval algorithm. These channels and their uses are described in detail in Susskind et al (2014a). The channels shown in yellow in Figure 3.2.1 are those used to determine the vector  $\eta$ , and are also the same channels used in the retrieval of cloud fraction and cloud top pressure. The channels shown in red are the ones used in the determination of  $T(p)$ ; the channels shown in light blue are those used to determine  $T_s$  and shortwave surface spectral emissivity, and the channels shown in purple are those used to determine longwave surface spectral emissivity. Channels shown in other colors are used to determine the atmospheric humidity profile  $q(p)$ , and profiles of  $O_3$ ,  $CH_4$ , and  $CO$  as indicated in Figure 3.2.1. Some changes in the channel selections were introduced between Version 6 and Version 7, and the document *AIRS Version 7 Retrieval Channel Sets* lists all the channels used in the retrieval by function.

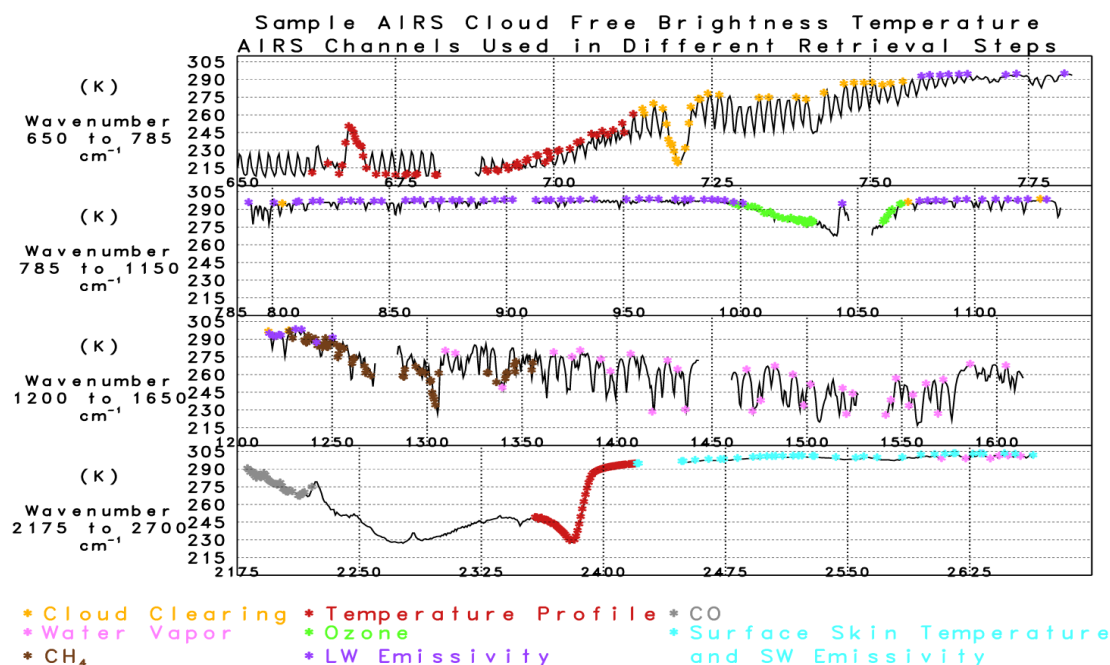


Figure 3.2.1. Channels used in the retrievals of the geophysical variables.



### 3.3 Initial Guess

The initial guess  $X_0$  in the AIRS version 6 and version 7 retrievals is generated by the Neural-Network methodology in place of the previously used two-regression approach (Susskind et al., 2011). The Neural-Network methodology involves the Stochastic Cloud Clearing/Neural Network (SCC/NN) (Blackwell, 2012; Blackwell and Milstein, 2014; Tao et al., 2013) algorithm, a statistical technique for performing temperature and water vapor retrievals from combined microwave and hyperspectral infrared observations. SCC/NN provides the first-guess temperature and water vapor profiles for Version 6 and 7 of the AIRS/AMSU Level 2 physical retrieval product (Susskind et al., 2014). The algorithm combines a statistical method for cloud clearing the radiance spectrum (Cho and Staelin, 2006), projected principal components (PPC) for efficient compression of the radiances correlated to the retrieved variables (Blackwell, 2005), and a feedforward neural network (Blackwell, 2005; W.J. Blackwell and Chen, 2009) for performing the retrievals from the cloud-cleared radiance PPCs. SCC/NN was implemented using radiances from the AIRS and AMSU instruments, and was trained using global training set derived from European Center for Medium-range Weather Forecasting (ECMWF) fields. The Version 6 and Version 7 algorithms, in part due to the incorporation of the SCC/NN first guess, have shown significantly improved yield in cloud-covered scenes and improved accuracy generally over the previous Version 5, which used a linear regression first guess (Blackwell and Milstein, 2014; Susskind et al., 2014, Yue and Lambrigtsen 2020).

The material in this ATBD chapter summarizes the SCC/NN algorithm, and is based on similar material that has appeared previously (Milstein, 2016).

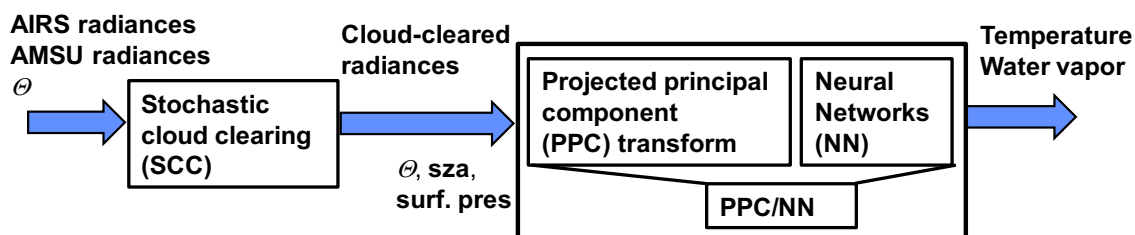


**Figure 3.3.1 Schematic of Stochastic Cloud Clearing / Neural Network (SCC/NN).**

### 3.3.1. SCC/NN Algorithm

A top-level diagram of SCC/NN algorithm is shown in Fig. 3.3.1. In a manner analogous to the physical retrieval, the stochastic cloud clearing (SCC) algorithm computes a single cloud-cleared infrared radiance spectrum for each field of regard (FOR) containing a 3x3 set of AIRS spectra over the measurement field of view (FOV). The cloud-cleared infrared radiances are then transformed using projected principal components, which best correlate to the retrieved variable. These PPCs of the cloud-cleared radiance, along with microwave measurements (when available) and other ancillary inputs (scan angle, solar zenith angle, and surface pressure), and are then used as inputs to the neural networks, which compute profiles of temperature and water vapor.

#### *Stochastic Cloud Clearing*

SCC (Cho and Staelin, 2006) is an algorithm for estimating the cloud-free infrared radiance spectrum from the 3x3 IR FOR, and, when available, the collocated microwave measurements. SCC utilizes variable cloud cover and contrast among neighboring IR FOVs along with the low cloud sensitivity of the microwave data to estimate cloud cleared IR radiances. The SCC is trained using measured radiances as input, and targets derived from synthetic clear-sky radiances, calculated from collocated ECMWF fields using the Stand-Alone Radiative Transfer Algorithm (SARTA) (Strow *et al.*, 2003). For surface emissivity, we followed Cho and Staelin (2006) in using the emissivity characteristics of ocean over both water and land. The authors reported little error introduced by this assumption due in part to the separate training of land and water regions, and algorithm's ability to compensate for such effects when they appear in both the training and testing sets. We also used a carbon dioxide profile that assumed a concentration of 370 ppm.

SCC estimates the cloud-cleared spectrum by performing a series of linear and nonlinear operations on the input, as shown in Fig. 3.3.2. The nine AIRS FOVs are sorted by cloudiness, and effective "warm" and "cold" IR spectra are selected and computed using the process described below. The inputs to SCC are seven noise-adjusted principal components (NAPCs) (Lee *et al.*, 1990) of the IR spectrum from the "warm" IR spectrum,

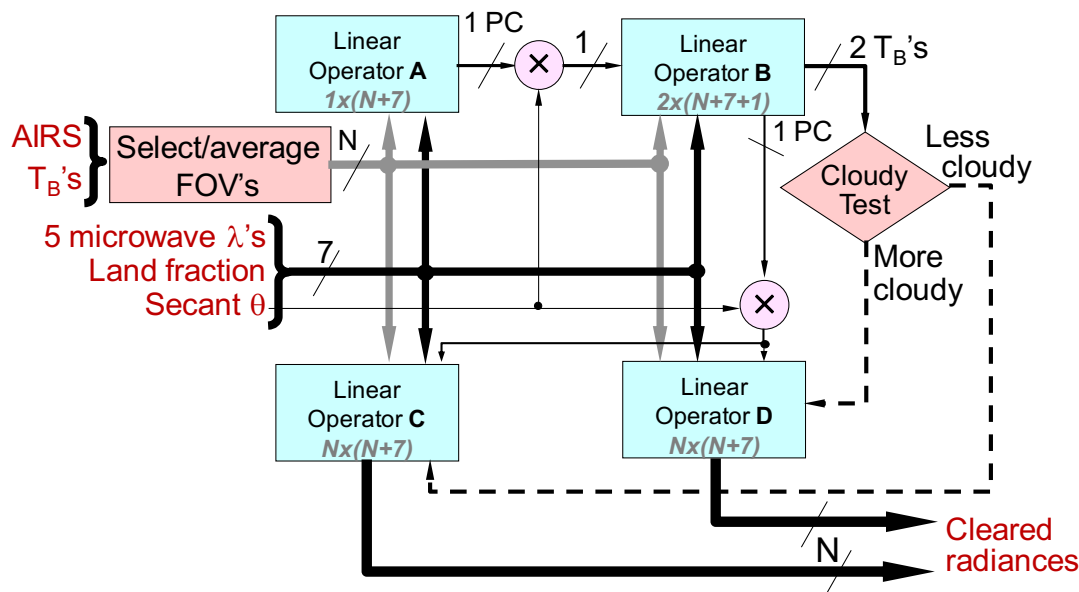


**Figure 3.3.2 Schematic of Stochastic Cloud Clearing algorithm.**

three NAPCs for the difference between the “warm” and “cold” spectra (based on IR channels whose weighting functions peak at low altitudes), a subset of the microwave brightness temperatures, the secant of the satellite scan angle, and the land fraction. First, a preliminary radiance correction to the “warm” spectrum is estimated using a regression linear operator **A**. (This correction is an intermediate quantity used to determine subsequent processing steps, but is not part of the final correction applied to the radiances.) The scalar output  $A_0$  is the first principal component (PC) of the cloud correction spectrum.  $A_0$  is multiplied by the secant of the scan angle, and combined with all the inputs to **A**, used as inputs to a second linear operator **B**, which outputs four PCs of a cloud correction to the “warm” spectrum. The PCs are used to compute radiance correction for two channels (4.5117  $\mu\text{m}$  and 4.4813  $\mu\text{m}$ ) with weighting function peak heights near 0.47 km and 2.7 km, respectively, low altitudes useful for determining cloudiness. A threshold test on both channels is used to classify the clearest averaged IR FOV into three categories, “30% least cloudy”, “80% least cloudy”, and “most cloudy”, with thresholds derived from the training set to meet those percentiles. For the “30% least cloudy” and “80% least cloudy” categories, two additional linear operators, **C** and **D** respectively, are used with the same inputs used for **B** to compute 4 PCs of a final cloud correction spectrum. The final correction spectrum is computed using the corresponding 4 PC vectors. For the “most

cloudy” category, the final cloud correction is the spectrum computed from **B**. The classification step, with different cloud correction applied based on cloudiness, along with the use of  $A_0 x \sec(\text{scan angle})$  as inputs to subsequent operations, provide simple ways of accommodating nonlinearity.

The “warm” and “cold” spectra used in the SCC algorithm inputs, are selected and computed as follows. The nine IR FOVs are sorted by cloudiness using the average radiance of channels between 4.16  $\mu\text{m}$  and 5  $\mu\text{m}$  with weighting-function peaks at heights between 1 and 3 km, with warmer FOVs assumed to be clearer. The “cold” spectrum is selected from the cloudiest FOV based on the sorting. Three different average “warm” spectra are created by selecting the clearest FOV spectrum, the average of the four clearest FOV spectra, and the average of all nine FOV spectra, respectively. For each of these three “warm” spectra, we compute a cloud correction as described above, with different versions of the operators (**A**, **B**, **C**, and **D**) trained and used for each. Afterward, the final averaged “warm” spectrum and cloud correction are constructed using the results for the clearest FOV for channels with weighting function peak height between 0 and 5 km, the results for the average of the four clearest FOVs for channels with weighting function peak height between 5 and 10 km, and the results for the average of all nine FOVs for all other channels.

### ***Projected Principal Components/Neural Network***

Neural networks (NNs) are represented by interconnected computational elements called nodes. In SCC/NN, they are used as a form of nonlinear regression, acting as function approximators trained to infer a statistical relationship between inputs and outputs from a training ensemble (*Blackwell, 2005; Blackwell and Chen, 2009*). Fig 3.3.3 shows the multilayer feed-forward NN structure used in SCC/NN, with an input layer, output layer, and one or two hidden layers. Each hidden layer contains nodes, which apply a hyperbolic tangent sigmoidal activation function.

$$z_j = \tanh(a_j) \quad (3.3.1)$$

where

$$a_j = \sum_{i=1}^d w_{ji} x_i + b_j \quad (3.3.2)$$

and  $x_i$  is the  $i^{\text{th}}$  input,  $z_j$  is the output of the  $j^{\text{th}}$  node, and  $w_{ji}$  and  $b_j$  are the weights and biases applied to the inputs. The output layer is linear. The weights and biases are the tuning parameters, which are optimized during the training process to minimize a sum-squared error cost function between the inputs and the training targets. The NNs used in SCC/NN were trained using the Levenberg–Marquardt optimizer, with gradients computed using the back-propagation algorithm. To avoid overfitting, early stopping was used based on network performance on a validation dataset (*Blackwell, 2005*).

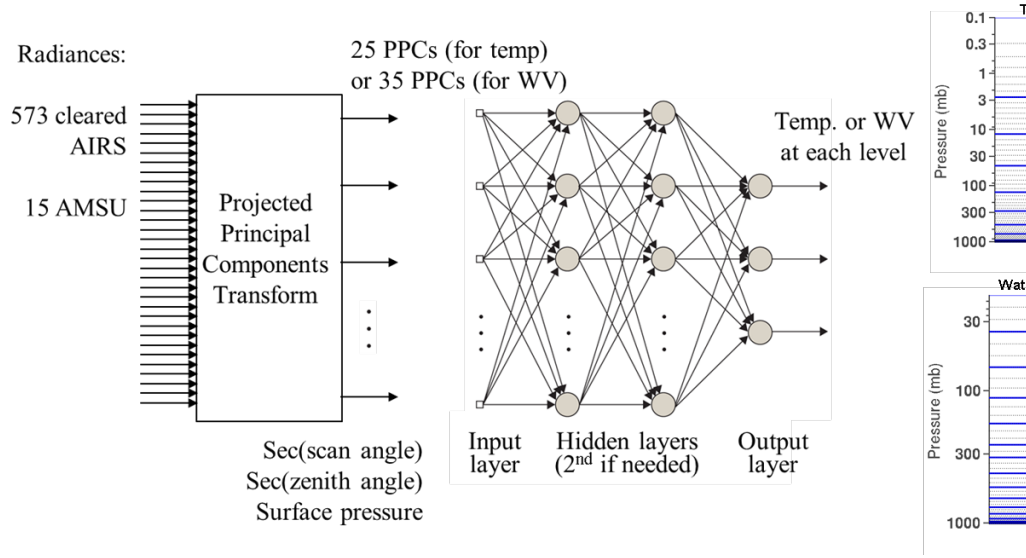


**Figure 3.3.3 Schematic of PPC-NN, the combination of compression and neural network algorithms.**

In the SCC/NN algorithm, the NN inputs are cloud-cleared radiances, compressed using the PPC transform, the microwave brightness temperatures, and ancillary inputs (the secant of scan angle, the secant of solar zenith angle, and the forecast surface pressure normalized by 1013 Mb). The projected principal component (PPC) transform has been shown to extract radiance information in each coefficient that is maximally correlated with the retrieved variable (*Blackwell, 2005*). The training targets are ECMWF reanalysis temperature, skin temperature, and water vapor mixing ratio fields at 60 sigma levels in V6 and 91 levels in V7 (pressure normalized by surface pressure), as described below.

We optimized the architecture of each NN based on empirical tradeoffs. For the temperature retrievals, we used 25 PPCs for the IR/microwave radiances. The original

ECMWF profile is subdivided into 9 vertical regions, shown in Fig. 3.3.3, with a NN dedicated to each region. Each NN output corresponds to retrieved temperature at a pressure level. The NN contains a single hidden layer with 20 hidden nodes. The same NN architecture is used to retrieve surface temperature as well. For water vapor, we used more radiance inputs and hidden nodes due to the greater nonlinearity of the retrieval. We used 35 radiance PPCs and two hidden layers, with 25 and 15 hidden nodes. We subdivide each profile into 15 vertical regions, shown in Fig. 3.3.3. The retrievals at the ECMWF pressure levels computed by the NNs are adapted to the 100-level AIRS support product levels by linearly interpolating, on a logarithm pressure-scale, from the sigma levels, facilitating their use by the AIRS Version 6 and Version 7 physical retrieval algorithm as a first guess. While the vertical regions used by the NN are not overlapping, significant discontinuities in profiles between vertical regions were not generally noted.

### ***Training Set and Stratification***

For both the SCC and NN algorithms, the training set was drawn from ECMWF temperature, skin temperature, and water vapor mixing ratio fields from every fourth day between December 1, 2004 and January 31, 2006 for Version 6. Version 7 expanded the training time period to include data from 2005, 2010, and 2013 in order to capture a wider range of climate variability. To assist in accommodating nonlinearity in the cloud clearing and NN retrievals, we stratify the radiance data and training targets using five variables: orbit node type (ascending and descending), latitude region (polar region north of 60°N, polar region south of 60°S, and remaining temperate/tropical region), season, and surface type. The surface type categories differ by latitude region, with category types determined in development based on empirical performance tradeoffs. For the temperate/tropical region the types are ocean and land, with land binned into eight categories according to surface pressure. These stratifications and categories are similar to those used by Cho and Staelin (2006) and were introduced in part to provide additional nonlinear capability for the SCC algorithm. For the North Pole region, the types are ocean, frozen ocean, and five categories of land binned by surface pressure. The South Pole region is similar but with seven land categories. These combinations of factors lead to a total of 200 stratifications. A different set of SCC and NN coefficients are trained and used in each stratification, where

each training set contains approximately 30,000 training profiles, along with 5,000 test profiles.

To avoid abrupt discontinuities over stratification boundaries, we use linear interpolation to gradually phase in transitions over the neighboring stratifications. For season transitions, we stratify using 5-month overlapping seasons, and linearly interpolate retrievals over season in the overlap interval. We also interpolate over latitude region with a 10 degree transition interval, and interpolate between land and ocean retrievals by using the land fraction as the interpolation weight. The global plots of SCC/NN results shown by Blackwell and Milstein (*Blackwell and Milstein*, 2014) demonstrate the lack of abrupt regional discontinuities.

In the polar regions, sea ice detection is needed to determine whether the “frozen ocean” surface type stratification should be used. Following the approach of Ferraro *et al.* (2005), we use AMSU measurements to compute sea ice concentration, and assume ice if this product exceeds a threshold (empirically chosen at 120%).

#### ***AIRS/AMSU Channels and Bad Channel Filling***

For AIRS, we selected 573 of the total 2378 channels to use in the SCC and NN algorithms, based on a combination of the 314 channels previously used by Cho and Staelin (2006) and additional channels historically used in AIRS retrievals (*Susskind et al.*, 2003). For AMSU, we use all channels as NN inputs, and channels 5, 6, and 8-10 as SCC inputs, prior to 2007. However, for 2007 onward, some AMSU channels have degraded (*Fetzer and Manning*, 2012), showing increased noise. Hence, our post-2007 retrieval approach uses all channels apart from 4, 5, and 7 as NN inputs, and use channels 2, 3, 6, and 8-10 as SCC inputs. For the AIRS V6 SCC/NN implementation used as the first guess to generate the L2 retrieval product, the post-2007 approach is used for all years, for consistency in the data record. An AIRS-only version of SCC/NN was also implemented to allow the AIRS v6 algorithm to degrade gracefully in the event of AMSU data being unavailable. This implementation uses the same algorithmic approach described above, but with AMSU data omitted as inputs. Sea ice is detected via a threshold test on forecast surface temperature in place of AMSU data, with the threshold, 271.3K, chosen based on prior AIRS team experience [*Olsen*, 2007].

Occasionally, an AIRS channel will be flagged by AIRS Level1B quality control flags at the granule or scanline level as having problems, such as “popping”, or estimated noise that significantly exceeds the expected levels. When a channel measurement or set of channel measurements is flagged, the SCC/NN implementation fills the “bad” channels with a predicted value obtained using linear regression on the remaining “good” AIRS channels, using previously computed covariance matrices for the radiances calculated from the training set inputs.

### *3.3.2 Differences between Version 7 and Version 6 SCCNN*

A new SCCNN algorithm version was developed and delivered as the AIRS Version 7 IR+MW and IR-only algorithm first guesses. The new SCCNN algorithm has been trained on newer, more diverse training sets. A series of versions with incremental changes during the Version7 development are summarized as the following:

- New coefficients trained on 2013-era ECMWF
- Increased training set comprehensiveness to capture a wide range of variability: trained using data from 2013, 2010, and 2005.
- Improved principal component representation for SCC algorithm, which improved cloud clearing results in IR-only algorithm.
- Improved SCCNN for V7 AIRS IR-only algorithm by including good channels in AMSU-A1
- Updated training set screening in which causes modest polar improvements.

## *3.4 Clear-Column Radiances*

Clouds have a significant effect on observed infrared radiances and can have non-negligible effects on microwave observations as well. Therefore, an accurate treatment of the effects of clouds on the observed AIRS radiances is critical to obtaining accurate soundings. There are three basic approaches for treating cloud effects on the infrared (IR) observations: (1) look for clear spots and therefore avoid the problem; (2) attempt to solve for the radiative effects of clouds directly in the inversion process; and (3) attempt to infer the radiances in the clear portions of the scene, called clear column radiance. The AIRS approach, based on methodology introduced by Chahine (1974, 1977), is the third. The advantage of this approach is that it does not have the clear-sky sampling bias of the first



approach, nor does it require the ability to accurately model the spectral emissive, reflective, and transmissive properties of the clouds, and their dependence on the vertical microphysics and geometry, as required by the second approach. The key assumption made in the third approach is that while there may be many types of clouds in the different FOVs, the radiative properties of a given type of cloud are identical in all FOVs within an FOR, which differ only in the relative amounts of these cloud types. Fields of view containing clouds with the same optical properties but at different heights, or clouds at the same height but with different optical properties, can be considered as having multiple cloud types. The other key assumption of this approach is that the FOVs have constant non-cloud characteristics in the clear portions of their scenes, with unknown temperature, humidity, etc.

Fundamental to the AIRS Science Team retrieval system is the generation of clear column radiances  $\hat{R}_i$  for each AIRS channel  $i$ .  $\hat{R}_i$  is determined for a channel as a linear combination of the radiances observed by that channel in each of the nine AIRS FOVs contained within the AMSU FOR, using coefficients that are channel independent (Susskind et al., 2003). Each AIRS FOV ( $j = 1, 9$ ) within the FOR has an observed radiance for each channel  $i$ ,  $R_{i,j}$ . The observations  $R_{i,j}$  are potentially affected by clouds in FOV  $j$ .  $\hat{R}_i$  represents the best estimate of what the observed AIRS channel  $i$  radiance, averaged over the nine FOV's in the AMSU FOR, would have been if all FOV's were completely cloud free. The  $\hat{R}_i$  is computed according to

$$\hat{R}_i = \bar{R}_i + \sum_{j=1}^9 \eta_j (\bar{R}_i - R_{i,j}) \quad (3.4.1)$$

where  $\bar{R}_i$  is the average value of  $R_{i,j}$  over the nine FOV's and  $\eta_j$  ( $j=1,9$ ) is a vector for each FOR which is derived as part of the retrieval process (Susskind et al., 2011). The physical retrieval process finds the surface and atmospheric state  $X$  such that computed radiances using  $X$  best match the derived clear column radiances  $\hat{R}_i$ .

As discussed in Susskind et al. (2011), the vector  $\eta$  is determined using observed radiances in a select set of  $I$  AIRS channels. If, for each channel  $i$ , one substitutes an estimate of  $R_{i,CLR}^\eta$  for  $\hat{R}_i^\eta$  in Equation 1, this gives  $I$  equations for 9 unknowns. The unconstrained weighted least square solution to this multilinear problem is given by

$$\eta = (\Delta R' N^{-1} \Delta R)^{-1} \Delta R' N^{-1} \Delta R_{CLR} \quad (3.4.2)$$

where  $\Delta R$  is an  $I \times 9$  matrix with  $\Delta R_{i,j} = \bar{R} - R_{i,j}$ ,  $\Delta R_{CLR}^n$  is an  $I \times 1$  matrix given by  $\Delta R_{i,CLR} = R_{i,CLR} - \bar{R}_i$ , and  $N$  is an  $I \times I$  channel noise covariance matrix.  $R_{i,CLR}$  is generated by computing expected clear sky radiances for cloud-clearing channel  $i$  based on a current estimate of the geophysical state  $X$ . As in Susskind et al. (2003, 2006), the solution for  $\eta$  is stabilized by solving for coefficients of up to the first four principal components of the matrix  $(\Delta R' N^{-1} \Delta R)$ . As shown in Equation 2, the vector  $\eta$  depends on the current estimate of the state vector  $X$ . The vector  $\eta$  is first determined using the state  $X$  coming from the initial guess, and subsequently recomputed using  $X$  coming from the first pass of the physical retrieval step. In general, the more accurate the state vector  $X$ , the more accurate the vector  $\eta$ , which is used to generate the clear column radiances  $\hat{R}_i$ .

Cloud-clearing theory (Chahine, 1974, 1977) says that to minimize the dependence of the final retrieved products on errors in the state vector  $X$ , and therefore achieve the best results cloud conditions where  $\hat{R}_i$  is more difficult to retrieve, longwave channels sensitive to cloud contamination should be used only in the determination of the coefficients  $\eta_j$  used in the generation of clear column radiances for all channels, and not be used for profile retrieval, or sounding. Sounding should be done using only shortwave channels if possible. In Version 5 (Susskind et al., 2011) tropospheric sounding  $15 \mu\text{m}$   $\text{CO}_2$  observations were used only in the derivation of the cloud clearing coefficients, and temperature profiles were derived using  $\hat{R}_i$  in channels in the  $4.3 \mu\text{m}$   $\text{CO}_2$  band, as well as in some stratospheric sounding  $15 \mu\text{m}$   $\text{CO}_2$  channels insensitive to clouds. This new approach allowed for the retrieval of accurate Quality Controlled values of  $\hat{R}_i$  and  $T(p)$  under more stressing cloud conditions than was achievable in Version 4, with a significant improvement in both the yield and the accuracy of retrieved temperature profiles (Susskind et al., 2011). Version 5 also included a new empirical approach to provide accurate case-by-case level-by-level error estimates for retrieved geophysical parameters as well as for channel-by-channel clear column radiances. Thresholds of these error estimates were used in a new approach for Quality Control in Version-5.

The AIRS Version 6 and Version 7 retrieval algorithm have further significant advances over Version 5. The basic theoretical approach used in newer versions to analyze AIRS/AMSU data is very similar to what was done in Version 5 with one major exception. As in Version 5, the coefficients used for generation of clear column radiances  $\hat{R}_i$  for all channels are determined in Version 6 and 7 using observed radiances only in longwave 15  $\mu\text{m}$  and 11  $\mu\text{m}$  channels and retrieved tropospheric temperatures using only  $\hat{R}_i$  in the AIRS shortwave 4.2  $\mu\text{m}$  CO<sub>2</sub> channels. Following cloud clearing theory, Version 6 and 7 use only observations in the shortwave window region 4.0  $\mu\text{m}$  – 3.76  $\mu\text{m}$  to simultaneously determine surface skin temperatures, along with shortwave surface spectral emissivity and surface bi-directional reflectance. Version 7 further omitted the temperature channels with cloud clearing corrections larger than 5K. Longwave surface spectral emissivity is retrieved in Version 6 and Version 7 in a subsequent step using values of  $\hat{R}_i$  only in the longwave window region. Version 5 did not follow this principle of doing retrievals using only shortwave channels, if possible, with regard to the surface parameter retrieval step. In Version 5,  $\hat{R}_i$  in both the longwave 8 - 12  $\mu\text{m}$  window region and in the shortwave 4.0  $\mu\text{m}$  – 3.7  $\mu\text{m}$  window region were used together to simultaneously determine surface skin temperature, surface spectral emissivity, and surface bi-directional reflectance of solar radiation. Another significant improvement found in Version 6 and Version 7 is the use of an initial guess for  $T^o(p)$  and  $q^o(p)$  generated by using Neural-Net methodology (Tao et al., 2011, Blackwell, 2011) in place of the previously used two-regression approach which provided the initial guess for these two geophysical parameters. These two modifications have resulted in significant improvements in the ability to obtain both accurate temperature profiles and surface skin temperatures under more stressing partial cloud cover conditions. Version 6 also uses an improved initial guess for land and ice surface spectral emissivity, as compared to what was used in Version 5. This also helped improve Version 6 land surface skin temperature retrievals. A separate document, *AIRS Version 7 Level 2 Cloud Cleared Radiances*, covers additional details about cloud cleared radiances and associated error estimates and quality control, for Version 7 and Version 6.

### 3.5 Surface Parameter Retrieval Methodology

The retrievals estimate ocean surface skin temperature  $T_s$ , ocean and land surface spectral emissivity  $\varepsilon_\nu$ , and global temperature profile  $T(p)$ . Only shortwave window channels are used in this retrieval step to simultaneously determine  $T_s$ , shortwave surface spectral emissivity,  $\varepsilon_{sw}(\nu)$ , and shortwave reflectivity,  $\rho_{sw}(\nu)$ . As with the determination of tropospheric temperature profile, use of only shortwave sounding channels is a superior approach to determine surface skin temperature because errors in cloud-clearing coefficients result in smaller errors in shortwave clear column brightness temperatures as compared to errors in using longwave brightness temperatures. In addition, shortwave window channel observations are much less sensitive to errors in the assumed water vapor profile than are longwave window observation.

The longwave surface spectral emissivity  $\varepsilon_{lw}(\nu)$  is solved in a subsequent step using only channels in the longwave window spectral region. This new step is performed after the humidity profile retrieval step because longwave window radiances can be very sensitive to the amount of atmospheric water vapor. In addition, Version 6 contains a new physical retrieval step, performed before the surface temperature retrieval step, in which  $\varepsilon_{sw}(\nu)$  is updated from its initial guess value. This additional step is performed only during the day because reflected solar radiation is not present at night.

The steps used in the Version 6 and Version 7 AO (AIRS only) algorithm are identical to those in the combined IR-MW retrieval. However, no AMSU-A observations are used in any step of the AO physical retrieval process; nor are they used in the QC methodology, which is otherwise analogous to that used in Versions 6 and 7. Also, no AMSU-A observations are used in any way in the generation of the AO Neural-Net initial state  $X_0$ , which uses coefficients that are trained separately from those of Versions 6 and 7 and are generated without any AMSU observations.

In addition to the separation of surface shortwave and longwave spectral emissivity retrievals into two steps, Versions 6 and 7 have improved other details in the retrieval of surface skin parameters. An improved form of the equation was used, which modifies the retrieved surface spectral emissivity  $\varepsilon(\nu)$  from its initial guess  $\varepsilon^0(\nu)$  and solve for  $\varepsilon(\nu)$  according to

$$(1 - \epsilon(\nu)) = (1 - \epsilon^0(\nu)) \left[ 1 + \sum_{k=1}^{k_{max}} A_k F_k(\nu) \right] \quad (3.5.1)$$

where there are  $k_{max}$  unknowns  $A_k$  to be solved for and  $F_k$  are piecewise linear functions of frequency, which vary from 0 to 4 for shortwave and 6 for longwave, respectively. Equation (3.5.1) is written in this multiplicative form so that  $\epsilon_i(\nu) = \epsilon^0(\nu)$  if all coefficients  $A_k$  are equal to zero.

The form of Eq. (3.5.1) is used both when solving for  $\epsilon_{sw}(\nu)$  in the shortwave emissivity retrieval step and when solving for  $\epsilon_{lw}(\nu)$  in the longwave surface emissivity step.

In the shortwave surface parameter retrieval step, in which  $\epsilon_i(\nu)$  is retrieved simultaneously with  $T_s$  and  $Q$ ,  $k_{max}$  is set equal to 4. The four shortwave functions  $F_k(\nu)$  have values equal to 1 at the four characteristic frequencies 2439.0, 2500.0, 2564.1, and 2631.6  $\text{cm}^{-1}$ , and equal to 0 at all other frequencies. A corresponding multiplicative form is used in Version 6 and Version 7 to modify the retrieval of surface shortwave reflectivity  $\rho(\nu)$  during the day according to

$$\rho(\nu) = \rho^0(\nu) \left[ \sum_{k=1}^4 B_k F_k(\nu) \right] \quad (3.5.2)$$

In the longwave surface emissivity step,  $k_{max}$  is set equal to 6, with analogous spectral shapes and corresponding characteristic frequencies of 769.23, 819.67, 877.19, 980.39, 1111.10, and 1204.80  $\text{cm}^{-1}$ .

Therefore, during the day, nine coefficients, one for  $\Delta T_s$ , where  $\Delta T_s$  is the difference of the retrieved value of  $T_s$  from its initial guess  $T_s^0$  and four values each of  $A_k$  and  $B_k$  are solved for in the shortwave surface parameter retrieval step, while five longwave parameters are solved for at night. The basic retrieval algorithm methodology uses the principal components of the information content matrix, on a case-by-case basis, and, thus, uses appropriate linear combinations of the functions  $F_k$  in Eqs. (3.5.1) and (3.5.2). Adding more functions  $F_k$  is not beneficial after a point, and becomes computationally costly. The numbers of functions used in Versions 6 and 7 in the shortwave and longwave surface emissivity retrieval steps were determined empirically according to retrieval performance.

The initial guess for surface spectral emissivity,  $\epsilon^0(\nu)$ , in both retrieval steps is set equal to the AIRS science team ocean emissivity model over nonfrozen ocean based on

Wu and Smith (1997). Over land and frozen ocean, we set equal  $\epsilon^0(\nu)$  to values interpolated from the  $1^\circ \times 1^\circ$  monthly mean MODIS science team aqua MODIS MYD11C3 V4.1 monthly gridded and interpolated emissivity for the year 2008. Spectral reflectance  $\rho^0(\nu)$  is initially set as  $(1 - \epsilon^0(\nu))/\pi$ , but is then modified in a subsequent Version 6/7 retrieval step performed immediately prior to the shortwave surface parameter retrieval step. In this step  $\rho^0(\nu)$  is updated in a one-parameter physical retrieval step, using the same channels as in the surface parameter retrieval step, according to

$$\rho^0(\nu) = [(1 - \epsilon^0(\nu))/\pi(1 + C)] \quad (3.5.3)$$

where  $C$  is a constant that scales  $\rho^0(\nu)$  but does not change its shape. This step helps account for the attenuation of incoming solar radiation by partial cloud cover along the path from the sun to the AIRS FOR. The values of  $\rho^0(\nu)$  shown in Eq. (3.5.3) are used as the initial guess in Eq. (3.5.2). Determination of this constant prior to the full surface retrieval step significantly improved retrieved  $T_s$ ,  $\epsilon(\nu)$ , and  $\rho(\nu)$  during daytime.

The term  $T_s$  represents surface skin temperature over all surfaces, while  $T_s$  over non-frozen ocean also represents Sea Surface Temperature (SST). In Susskind et al. (2014a), Version 6 retrievals of SST are compared against Version 5 retrievals and ECMWF forecasts. It is shown that quality controlled SST retrievals accept considerably more cases in Version 6 than in Version 5, and also show better agreement with the ECMWF forecasts. Susskind et al. (2014a) also compare Version 6 ocean surface spectral emissivity to Version 5 retrievals and ECMWF forecasts. Version 6 shows improvement from Version 5 in terms of removal of spurious features, as well as stability and accuracy when compared with ECMWF. Susskind et al. (2014a) also shows that land surface emissivity retrievals are considerably more accurate in Version 6 than in Version 5. It is impractical to validate land surface skin temperatures on a global scale because  $T_s$  over land changes very rapidly in space and time.

### ***3.7. Difference Between Surface Skin Temperature and Surface Air Temperature***

Surface air temperature is a basic climatological variable and plays a major role in synoptic meteorology. It is measured at a large number of stations, but their spatial density is highly variable and their distribution is limited primarily to mid-latitude northern

hemisphere land. Knowledge of the air temperature at high spatial resolution is of great importance to understanding weather and climate over different spatial scales. Surface skin temperature is a basic quantity needed to determine the Earth's radiation emitted from the surface. The radiative heating of the surface and the subsequent heat flux towards the lower atmosphere through conduction and convection results in a strong relationship between surface skin temperature and air temperature in the boundary layer. We refer to  $(T_s - T_{surf})$ , the difference between surface skin temperature and surface air temperature, as  $\Delta T_{s,a}$ .  $\Delta T_{s,a}$  depends on spatial conditions such as altitude, topography, and land surface type. It also depends on temporal conditions such as season and time of the day. Susskind et al. (2014b) present an overview of the global distribution of  $\Delta T_{s,a}$  as depicted by the AIRS Version-6 level 3 data set. They compare annual and seasonal mean climatologies of  $T_s$ ,  $T_{surf}$ , and  $\Delta T_{s,a}$ , as well as their interannual variability. They found that annual mean surface skin temperature is about 1 K warmer than the surface air temperature over land, especially in arid areas for daytime (1:30 p.m.), with opposite sign of the difference for nighttime (1:30 a.m.). Oceanic surface skin temperatures also tend to be warmer than surface air temperatures in the midlatitudes for all times. Polar surface skin temperatures are colder than surface air temperatures (by about 1 K) except over open ocean.

### 3.8. Retrieval of Cloud Fraction and Cloud Top Pressure

The radiatively effective cloud fraction at frequency  $\nu$ ,  $\alpha\epsilon_\nu$ , is the product of  $\alpha$ , the geometric fractional cloud cover of an AIRS FOV as seen from above, and  $\epsilon_\nu$  the cloud spectral emissivity. The AIRS Science Team cloud parameter retrieval methodology (Susskind et al., 2003, Susskind et al., 2011) determines  $\alpha\epsilon_\nu$ , the product of these two terms but not the separate components, along with a corresponding cloud top pressure  $p_c$ , for each of up to two layers of clouds in a given scene. The quantity  $\alpha\epsilon_\nu$  is referred to as ‘cloud fraction’. A basic simplifying assumption of the cloud retrieval methodology used in Versions 5, 6 and 7 is that the clouds are gray, that is that  $\epsilon_\nu$  and so  $\alpha\epsilon_\nu$  are independent of frequency. Version 5 simultaneously derived 20 parameters for each of nine AIRS fields of view within the AMSU field of regard: nine effective cloud fractions  $\alpha\epsilon_1$  and  $\alpha\epsilon_2$ , one pair for each AIRS field of view  $j$ , along with two cloud top pressures  $p_{c1}$ , and  $p_{c2}$  considered to be representative of the pressures of each of the two layers of clouds covering

the entire AMSU field of regard. In Versions 6 and 7 the cloud parameter retrieval step is performed separately for each AIRS FOV  $j$  to determine nine sets of  $\alpha\varepsilon_{1,j}$ ,  $\alpha\varepsilon_{2,j}$ ,  $p_{c1,j}$ , and  $p_{c2,j}$ . The total radiatively effective cloud fraction for a set of nine AIRS fields of view,  $\alpha\varepsilon$ , is computed as the average cloud fraction according to

$$\alpha\varepsilon = \sum_{j=1}^9 (\alpha\varepsilon_{1,j} + \alpha\varepsilon_{2,j}) / 9 \quad (3.8.1)$$

and an effective cloud top pressure for the AIRS field of regard is computed as the cloud fraction-weighted average of all nine values of  $p_{c1}$  and  $p_{c2}$  in the AIRS field of regard

$$p_c = \sum_{j=1}^9 (\alpha\varepsilon_{1,j} p_{c1,j} + \alpha\varepsilon_{2,j} p_{c2,j}) / \sum_{j=1}^9 (\alpha\varepsilon_{1,j} + \alpha\varepsilon_{2,j}) \quad (3.8.2)$$

as was also done in Version 5. The Version 6 and 7 Level 2 products contain estimates of  $\alpha\varepsilon_{1,j}$ ,  $\alpha\varepsilon_{2,j}$ ,  $p_{c1,j}$ ,  $p_{c2,j}$  for each AIRS field of view, as well as the single AMSU field of regard heritage values  $\alpha\varepsilon$  and  $p_c$  defined according to Equations 3.8.1 and 3.8.2.

Cloud parameters in an AIRS field of view are derived such that channel radiances  $R_i(\alpha\varepsilon_1, \alpha\varepsilon_2, p_{c1}, p_{c2}, X)$  computed using these cloud parameters and state  $X$  (temperature, water vapor, etc.) for the field of view, best match the observed radiances in that field of view for a set of cloud retrieval channels. The channels used to determine cloud fraction and cloud top pressure are the same as those used in the cloud clearing step and are shown in Fig. 3.2.1. The state vector  $X$  used to derive cloud parameters in an AIRS field of view is the geophysical state retrieved for the entire AIRS set of nine fields of view.

A complication in the cloud parameter retrieval methodology is that the least squares fit may result in nonphysical cloud parameter solutions. To avoid nonphysical results, retrieved cloud fractions are constrained to  $[0,1]$ , and cloud top pressures very close to the surface or above the tropopause are excluded. Because of the way these constraints were handled in Version 5, many cloud retrievals in Version 5 failed to converge properly. Numerous enhancements in Versions 6 and 7 stabilized the cloud parameter retrieval step and also allowed for cloud top pressures closer to the surface than was allowed in Version 5.

No changes have been made to the Version 7 cloud parameter retrievals although there are small differences between Version 6 and Version 7 cloud parameters, especially



for FOVs with effective cloud fractions less than 0.05, near the sensitivity threshold of AIRS.

More details about the cloud parameter retrieval step in Versions 5, 6, and 7 are given in Susskind et al. (2014a). That study also show that the spatial distribution of retrieved cloud fraction and cloud top pressure is much more realistic in Version 6 than in Version 5, especially for stratus cloud cover off the west coasts of continents. Kahn et al. (2014) give more details about the updates to the cloud parameter retrieval algorithm in Version 6 as compared to Version 5, and show that the higher spatial resolution cloud top pressures, and corresponding cloud top pressures found in Version 6, have coherent spatial structure and contain a larger range of values than is found in Version 5. Kahn et al. (2014) also show a much better agreement of retrieved Version 6 cloud parameters, as compared to Version 5, with those found in CloudSat and CALIOP data. That study describes the new Version 6 products of cloud thermodynamic phase, ice cloud effective diameter, and ice cloud optical thickness, which are derived on an AIRS FOV basis using other AIRS retrieved products as a starting point for their radiative transfer calculations.

### 3.9. *Computation of Outgoing Longwave Radiation and Clear-Sky OLR*

OLR is determined primarily by the earth's skin surface temperature,  $T_s$ ; skin surface spectral emissivity,  $\varepsilon_v$ ; atmospheric vertical temperature profile,  $T(p)$  and water vapor profile,  $q(p)$ ; and the heights, amounts, and spectral emissivities of cloud layers. OLR also depends on the vertical distributions of trace gases such as  $O_3(p)$ ,  $CH_4(p)$ ,  $CO_2(p)$ , and  $CO(p)$ . In Version-5, OLR was computed for each AIRS FOV  $j$  (Mehta and Susskind, 1999a,b) as the sum of fluxes in 14 contiguous spectral bands  $m$ , allowing for up to two levels of clouds as seen from above, according to

$$F_\ell = \sum_{m=1}^{14} F_m = \sum_{m=1}^{14} [(1 - \alpha\varepsilon_{1,j} - \alpha\varepsilon_{2,j})F_{m,CLR} + \alpha\varepsilon_{1,j}F_{m,CLD1} + \alpha\varepsilon_{2,j}F_{m,CLD2}] \quad (3.9.1)$$

where  $F_{m,CLR}$  is the computed clear sky flux to space integrated over all angles and in spectral band  $m$ ;  $F_{m,CLDn}$  is the analogous computed flux emanating from an opaque cloud

at cloud top pressure  $p_{cn}$ ; and  $\alpha\epsilon_n$  is the radiatively effective cloud fraction for the cloud at pressure  $p_{cn}$ .

The clear sky flux in spectral band  $m$  was computed according to

$$F_{m,CLR} = \pi \left[ \epsilon_m B(\nu_m, T_s) \tau_m(p_s) + \int_{\ln p_s}^{\ln \bar{p}} B(\nu_m, T(p)) \frac{d\tau_m(p)}{d\ln p} d\ln p \right] \quad (3.9.2)$$

where  $B(\nu, T)$  is the Planck blackbody function evaluated at temperature  $T$  and frequency  $\nu_m$ , the central frequency of spectral band  $m$ . Here  $\epsilon_m$  is the mean surface emissivity in band  $m$ , and the term  $\tau_m(p)$  represents the effective band averaged atmospheric transmittance in band  $m$  from pressure  $p$  to the top of the atmosphere  $\bar{p}$ .  $F_{m,CLDN}$  was computed in an analogous manner, but by replacing  $T_s$  by the cloud top temperature  $T(p_n)$ ;  $p_s$  by  $p_{cn}$ ; and the surface emissivity  $\epsilon_m$  by a cloud emissivity which is assumed to be equal to unity. Mehta and Susskind (1999a, 1999b) parameterized  $\tau_m(p)$  as a function of temperature, moisture, and ozone profile. The spectral bands used in Equation (3.9.2) in Version 5 ranged from  $2 \text{ cm}^{-1}$  through  $2750 \text{ cm}^{-1}$ . The clear sky OLR,  $OLR_{CLR}$ , is also a product computed in Version 5 for each AMSU FOR, obtained by setting both  $\alpha\epsilon_1$  and  $\alpha\epsilon_2$  to zero in Equation (3.9.1).

Geophysical parameters are retrieved from AIRS radiance observations under both cloud-free and cloudy conditions, though their quality is poorer under very cloudy conditions, especially at or near the surface. For this reason, the AIRS Version-5  $OLR_{CLR}$  product for a given FOR was included in the generation of the Level 3 monthly mean gridded  $OLR_{CLR}$  product only for those cases in which the AIRS retrieved cloud fraction was less than 90%, and which passed an additional  $OLR_{CLR}$  quality control procedure indicating the retrieval is of acceptable accuracy down to the surface (Susskind et al., 2011). Susskind et al. (2012) showed that while Version-5 OLR was biased high compared to CERES OLR by about  $7 \text{ W/m}^2$ , anomalies and short-term trends of AIRS Version 5 OLR over the period September 2002 through June 2011 were very close to those obtained using CERES observations, even down to the  $1^\circ$  spatial scale.

AIRS Version 6 and 7 use an improved RTA in the computation of OLR (Iacono et al., 2008). Computation of OLR in Version 6 and 7 is very similar to that in Version 5,

with the minor difference that 16 spectral bands, whose spectral intervals are shown in Table 3.9.1 are used in the Version 6 and 7 OLR RTA as opposed to the 14 bands used in Version 5. This new OLR RTA also has two upgrades compared to Mehta and Susskind (1999a, 1999b). Most significantly, the new OLR RTA uses updated line absorption parameters, especially in the very strong water vapor absorption band near  $300\text{ cm}^{-1}$ . In addition, unlike in Version 5, the Version 6 and 7 OLR RTA allows for variations in space and time of profiles of  $\text{CO}_2$ ,  $\text{CO}$ ,  $\text{CH}_4$ , and  $\text{N}_2\text{O}$ . Version 6 and 7 OLR includes products for each of the sixteen spectral components of OLR shown in Table 3.9.1. In Version 6 and 7, the total OLR for a given AIRS field of view is assigned the same QC value as the retrieved cloud parameters. The Level 3 OLR product uses all cases with QC=0 or QC=1, with a yield of close to 100%. The Version 6 and 7 QC flags for  $\text{OLR}_{\text{CLR}}$  and total precipitable water vapor  $W_{\text{TOT}}$  are set equal to the QC flag for  $T(p_s)$ . Consequently, the Level 3  $\text{OLR}_{\text{CLR}}$  product contains exactly the same cases as those included in the generation of the  $T(p_s)$  and  $W_{\text{TOT}}$  Level 3 products, with a global yield of about 80%.

AIRS Version 6 OLR products are discussed in Susskind et al. (2014a). The OLR difference between Version 7 and Version 6 and their comparison with CERES are shown in the *AIRS Version 7 Level 2 Performance Test and Validation Report*.

## 4. ERROR ESTIMATES AND QUALITY CONTROL FLAGS

This section describes the general methodology for estimating errors and setting Quality Control (QC) flags. The document *AIRS Version 7 Level 2 Cloud Cleared Radiances* provides additional theoretical background, descriptions of the methodology, and analyses of the resulting error estimates for cloud properties and for cloud cleared radiances. The criteria for setting QC flags and for estimating errors associated with other AIRS retrieved quantities are detailed in the document *AIRS/AMSU/HSB Version 7 Level 2 Quality Control and Error Estimation*.

Each retrieved quantity  $X$  in Versions 5, 6 and 7 has an associated error estimate  $\delta X$ . A major advancement in Version 5 was the development of a methodology to generate empirical error estimates, and to use thresholds of these error estimates for QC purposes. Analogous procedures are also used in Versions 6 and 7 with some modifications. Version-4 used 12 internal threshold value tests for generating QC flags for different geophysical parameters (Susskind et al., 2006). Version 5 used the case-by-case values of these 12 internal tests, in addition to those of 4 other tests, as error estimate predictors to generate case-by-case error estimates  $\delta X$  for select geophysical parameters  $X$  (Susskind et al., 2011). Versions 6 and 7 use an analogous methodology to that of Version 5 to generate empirical error estimates  $\delta X$ , with some modifications resulting from changes in the steps used in the Versions 6 and 7 retrieval system compared to those used in Version 5. Susskind et al. (2014a) describe in detail how error estimates are generated and used for QC purposes in both Versions 5 and 6.

In Versions 6 and 7, error estimates for most geophysical parameters  $X_j$  are computed by taking a linear combination of error estimate predictors

$$\delta X_j^m = \left| \sum_{n=1}^N M_{jn}^X Y_n^m \right| \quad (4.1)$$

where  $\delta X_j^m$  is the error estimate of retrieved geophysical parameter  $X_j$  for case  $m$ ,  $Y_n^m$  is the value of the  $n^{th}$  error estimate predictor for case  $m$ ,  $M$  is a matrix defined below, and  $N$  is the number of predictors used to determine the error estimates. All error estimates are positive by definition. Values of the predictors are all positive and larger values of  $Y_n^m$  generally indicate that a poorer retrieval will be obtained for case  $m$ .

The coefficients of  $M^X$  are determined in essentially the same manner in Version 6 and 7 as was done in Version 5. In Versions 6 and 7, six distinct matrices  $M^X$  have been generated for separate use under daytime or nighttime, as well as for separate use over 1) non-frozen ocean; 2) non-frozen land; and 3) frozen (ice or snow) cases. (In Version 5, only four such matrices were used, in which a single pair of matrices (day or night) was used to be representative of all cases not classified as non-frozen ocean, and a separate pair of matrices was used over non-frozen ocean.) See *AIRS/AMSU/HSB Version 7 Level 2 Quality Control and Error Estimation* for additional details on error estimate predictors.

The coefficients of the matrix  $M^X$  can be determined in a straightforward manner if one is given the true values of  $X$ ,  $X^{truth}$ , for a representative ensemble of cases.  $M^X$  is determined by finding the coefficients that minimize the RMS difference of  $(\Delta X_j^m - \delta X_j^m)$ , where  $\Delta X_j^m = (X_j - X_j^{truth})^m$ , when  $M^X$  is used in Equation 4.1 to generate  $\delta X_j^m$ . The  $N$  coefficients of  $M_{jn}^X$  are determined separately for each parameter  $\delta X_j$ . In order to generate the Version 6 coefficients for each of the six different matrices  $M$ , we use appropriate spatial subsets of  $X_j^m$  and  $Y_n^m$ , generated using all Version 6 retrievals on September 29, 2004 and February 24, 2007, along with the collocated ECMWF 3-hour forecast values of  $X_j^m$ , which were taken to be  $X_j^{truth}$ . The coefficients of the six sets of matrices  $M$  were determined separately for Version 6 and 7, and for Version 6 and 7 AIRS Only, each based on observations on these two days, and these coefficients are then used for all time periods.

## APPENDIX: ABBREVIATIONS AND ACRONYMS

AIRS	Atmospheric Infrared Sounder
AIRS-RTA	AIRS Radiative Transfer Algorithm
AMSR-E	Advanced Microwave Scanning Radiometer-EOS
AMSU	Advanced Microwave Sounding Unit
AMSU-A	Advanced Microwave Sounding Unit-A (20-channel MW radiometer)
AMSU-B	Advanced Microwave Sounding Unit-B (5-channel MW radiometer)
ATBD	Algorithm Theoretical Basis Document
AVHRR	Advanced Very High Resolution Radiometer
C	degrees Centigrade
COLR	Clear Sky Outgoing Radiation
DAAC	Distributed Active Archive Center
DB, dB	decibel
EOF	Empirical Orthogonal Functions
EOS	Earth Observing System
ER-2	Earth Research-2 (NASA's civilian version of Lockheed Skunkworks U-2)
ESDIS	Earth Science Distributed Information System
FOR	Field of Regard
FOV	Field of View
FTS	Fourier Transform Spectrometer
FWHH	Full Width Half Height
GHz	Gigahertz ( $10^9$ Hertz, or cycles/second)
GSFC	Goddard Space Flight Center
HITRAN	High Resolution Transmission Molecular Absorption Database
HSB	Humidity Sounder of Brazil

## AIRS V6 & V7 L2 ATBD

IMG	Infrared Monitor for Greenhouse Gases
IR	infrared
IRIS	Infrared Interferometer Spectrometer
JPL	Jet Propulsion Laboratory
K	Kelvins
kCARTA	kCompressed Atmospheric Radiative Transfer Algorithm
km	kilometer ( $10^3$ meters)
kPa	kilopascal ( $10^3$ pascal, equivalent to 10 bar)
L0-L4	Level 0 through Level 4 (processing)
MHS	Microwave Humidity Sounder
mm	micrometer, micron ( $10^{-6}$ meter)
MODIS	Moderate Resolution Imaging Spectroradiometer
MPM87	Millimeter-wave Propagation Model (Liebe and Layton, 1987)
MPM89	Millimeter-wave Propagation Model (Liebe, 1989)
MPM92	Millimeter-wave Propagation Model (Liebe, et al, 1992)
MPM93	Millimeter-wave Propagation Model (Liebe, et al, 1993)
MSU	Microwave Sounder Unit
MW	microwave
NASA	National Aeronautics and Space Administration
NCEP	National Center for Environmental Prediction
NEDT	Noise Equivalent Temperature Difference
NEDT	Noise Equivalent Temperature Difference
NEMS	Nimbus-E Microwave Sounder
NESDIS	National Environmental Satellite Data and Information Service
NEXRAD	Next Generation Radar

## AIRS V6 & V7 L2 ATBD

NN	Neural Network
NOAA	National Oceanic and Atmospheric Administration
OLR	Outgoing Longwave Radiation
PCs	Principle Components
PCSs	Principle Components Scores
PGE	Product Generation Executive
QC	Quality Control
QA	Quality Assessment
OPTRAN	Optical Path TRANsmittance
RH	Relative Humidity
RMS	Root Mean Square
RTA	Radiative Transfer Algorithm
SCC/NN	Stochastic Cloud Clearing/Neural Network
SDPS	Science Data Processing System
SIRS	Satellite Infrared Radiation Spectrometer
SRF	Spectral Response Function
SSM/T2	Special Sensor Microwave/Water Vapor Profiler
SST	Surface Skin Temperature
SVD	Singular Value Decomposition
THz	Terahertz ( $10^{12}$ Hertz)
TIGR	TOVS Initial Guess Retrieval
TIROS	Television Infrared Observation Satellite
TLSCF	Team Leader Science Computing Facility
TPW	Total Precipitable Water
TOVS	TIROS Operational Vertical Sounder
VTPR	Vertical Temperature Profile Radiometer



## REFERENCES

- Aumann, H.H. , M.T. Chahine, C. Gautier, M. Goldberg, E. Kalnay, L. McMillin, H. Revercomb, P.W. Rosenkranz, W. L. Smith, D. H. Staelin, L. Strow and J. Susskind, (2003a), “AIRS/AMSU/HSB on the Aqua Mission: Design, Science Objectives, Data Products and Processing Systems,” *IEEE Trans. Geosci. Remote Sens.*, Vol.41, 253-264.
- Bauer, A., Godon, M., Kheddar, M., and Hartmann, J.M., 1989: Temperature and Perturber Dependences of Water Vapor Line-Broadening. Experiments at 183 GHz; Calculations Below 1000 GHz, *J. Quant. Spectrosc. Radiat. Transfer*, **41**, 49-54.
- Bauer, A., Godon, M., Carlier, J., Ma, Q., and R.H. Tipping, 1993: Absorption by H<sub>2</sub>O and H<sub>2</sub>O-N<sub>2</sub> Mixtures at 153 GHz, *J. Quant. Spectrosc. Radiat. Transfer*, **50**, 463-475.
- Bauer, A., Godon, M., Carlier, J., and Ma, Q., 1995: Water Vapor Absorption in the Atmospheric Window at 239 GHz, *J. Quant. Spectrosc. Radiat. Transfer*, **53**, 411-423.
- Blackwell, W. J., and F. W. Chen (2009), *Neural Networks in Atmospheric Remote Sensing*, Artech House, Incorporated.
- Blackwell, W. J., “Neural network Jacobian analysis for high-resolution profiling of the atmosphere,” *EURASIP Journal on Advances in Signal Processing*, 2012:71 doi:10.1186/1687-6180-2012-71 (2012).
- Blackwell, W. J., and A. B. Milstein (2014), A Neural Network Retrieval Technique for High-Resolution Profiling of Cloudy Atmospheres, *IEEE J. Sel. Top. Appl. Earth Obs. Remote Sens.*, 7(4), 1260-1270.
- Cho, C., and D. H. Staelin (2006), Cloud clearing of Atmospheric Infrared Sounder hyperspectral infrared radiances using stochastic methods, *J. Geophys. Res, D, Atmos.*, *111*(D9), 10 pp.
- Gamache, R.R., J.-M. Hartmann, and L. Rosenmann, 1994: Collisional broadening of water vapor lines- 1. A survey of experimental results. *J. Quant. Spectrosc. Radiat. Transfer*, **52**, 481-499.
- Chahine, M. T., “Remote sensing of cloudy atmospheres. I. The single cloud layer,” *J. Atmos. Sci.*, 31, 233-243 (1974).

- Chahine, M. T., “Remote sensing of cloudy atmospheres. II. Multiple cloud formations,” *J. Atmos. Sci.*, **34**, 744-757 (1977).
- Chedin, A., N. A. Scott, C. Wahiche, and P. Moulinier, 1985: The improved initialisation inversion method: A high resolution physical method for temperature retrievals from the TIROS-N series. *J. Clim. Appl. Meteor.*, **24**, 128-143.
- Fetzer, E., and E. Manning (2012), Failure of AMSU-A Channel 4 and Degradation of AMSU-A Channel 5 NeDT Affecting AIRS Retrieval Performance, edited.
- Godon, M., Carlier, J. and Bauer, A., 1992: Laboratory Studies of Water Vapor Absorption in the Atmospheric Window at 213 GHz, *J. Quant. Spectrosc. Radiat. Transfer*, **47**, 275-285.
- Iacono, M. J., J. S. Delamere, E. J. Mlawere, M. W. Shephard, S. A. Clough, and W. D. Collins, “Radiative forcing by long-lived greenhouse gases: Calculations with the AER radiative transfer models,” *J. Geophys. Res.*, **113**, D13103, doi:10.1029/2008JD009944 (2008).
- Kahn, B. H. et al., “The Atmospheric Infrared Sounder Version 6 Cloud Products,” *Atmos. Chem. Phys.*, **14**, 399-426 (2014).
- Lee, J. B., A. S. Woodyatt, and M. Berman (1990), Enhancement of high spectral resolution remote-sensing data by a noise-adjusted principal components transform, *Geoscience and Remote Sensing, IEEE Transactions on*, **28**(3), 295-304.
- Liebe, H.J., Thompson, M.C. Jr., and Dillon, T.A., 1969: Dispersion Studies of the 22 GHz Water Vapor Line Shape, *J. Quant. Spectrosc. Radiat. Transfer*, **9**, 31-47.
- Liebe, H.J. and Dillon, T.A., 1969: Accurate Foreign-Gas-Broadening Parameters of the 22-GHz H<sub>2</sub>O Line from Refraction Spectroscopy, *J. Chem. Phys.*, **50**(2), 727-732 (1969).
- Liebe, H.J., and Layton, D.H., Millimeter-Wave Properties of the Atmosphere: Laboratory Studies and Propagation Modeling, NTIA Report 87-224, October 1987.
- Liebe, H.J., Hufford, G.A., and Manabe, T., 1991: A Model for the Complex Permittivity of Water at Frequencies Below 1 THz, *Int. J. of Infrared and Mill. Waves*, **12**(7), pp. 659-675

- Liebe, H.J., Rosenkranz, P.W., and Hufford, G.A., 1992: Atmospheric 60-GHz Oxygen Spectrum: New Laboratory Measurement and Line Parameters, *J. Quant. Spectrosc. Radiat. Transfer*, **48**(5/6), 629-643
- Loeb et al., "Toward optimal closure of the Earth's top-of-atmosphere radiation budget," *J. Climate*, 22, 748-766, doi:10.1175/2008JCLI2637.1 (2009).
- McMillin, L. M., and Crone, L. J., and Kleespies, T. J., Atmospheric transmittance of an absorbing gas: Improvements to the OPTRAN approach. *Applied Optics*, **34**, 8396-8399, 1995.
- Mehta, A. V. and J. Susskind, "Outgoing Longwave Radiation from the TOVS Pathfinder Path A data set", *J. Geophys. Res.*, 104, 12193-12212, (1999a).
- Mehta, A. V. and J. Susskind, "Longwave Radiative Flux calculations in the TOVS Pathfinder Path A data set." NASA Tech. Rep., GSFC/CR-1999-208643 (1999b).
- Milstein, A. B., and Blackwell, W. J. (2016), Neural network temperature and moisture retrieval algorithm validation for AIRS/AMSU and CrIS/ATMS, *J. Geophys. Res. Atmos.*, 121, 1414– 1430, doi:[10.1002/2015JD024008](https://doi.org/10.1002/2015JD024008).
- Mo, T., "AMSU-A antenna pattern corrections," *IEEE Trans. Geosci. Rem. Sens.*, **37**, 103-112 (1999).
- Olsen, T. J. H. a. E. T. (2007), AIRS/AMSU/HSB Version 5 Level 2 Performance and Test Report *Rep.*, Jet Propulsion Laboratory, Pasadena, CA.
- Poynter, R.L. and Pickett, H.M., 1985: Submillimeter, Millimeter, and Microwave Spectral Line Catalog, *Applied Optics*, **24**(14), pp. 2235-2240.
- Rodgers, C. D., 2000: Inverse Methods for Atmospheric Sounding: Theory and Practice, World Scientific Publishing, Singapore.
- Rothman, L. S., C. P. Rinsland, A. Goldman, S. T. Massie, D. P. Edwards, J.-M. Flaud, A. Perrin, C. Camy-Peyret, V. Dana, J.-Y. Mandin, J. Schroeder, A. McCann, R. R. Gamache, R. B. Wattson, K. Yoshino, K. V. Chance, K. W. Jucks, L. R. Brown, V. Nemtchinov, P. Varanasi, 1998: "The HITRAN Molecular Spectroscopic Database and HAWKS (HITRAN Atmospheric WorkStation):1996 Edition," *J. Quant. Spectrosc. Radiat. Transfer* **60**, 665-710.

- Rosenkranz, P. W., 1998: Water vapor microwave continuum absorption: A comparison of measurements and models. *Radio Science*, **33**, 919-928. (Correction, *Radio Science*, **34**, 1025, 1999).
- Rosenkranz, P. W., and C. D. Barnet, 2006: "Microwave radiative transfer model validation", *J. Geophys. Res.*, **111**, D09S07, doi:10.1029/2005JD006008.
- Schwartz, M. J., 1997: Observations and Modeling of Atmospheric Oxygen Millimeter-wave Transmittance, Ph.D. Thesis, Mass. Inst. Of Tech., Dept. of Physics, Cambridge, MA.
- Strow, L., and Hannon, S., and DeSouza-Machado, S., and Motteler, H., An Overview of the AIRS Radiative Transfer Model. *IEEE Transactions on Geosciences and Remote Sensing*, **41**, No. 2, 303-313, 2003.
- Susskind, J., C. D. Barnet, and J. M. Blaisdell, "Retrieval of atmospheric and surface parameters from AIRS/AMSU/HSB data in the presence of clouds," *IEEE Trans. Geoscience and Remote Sensing*, **41**, 390-409, DOI: 10.1109/TGRS.2002.808236 (2003).
- Susskind, J., C. Barnet, J. Blaisdell, L. Iredell, F. Keita, L. Kouvaris, G. Molnar, and M. Chahine, "Accuracy of geophysical parameters derived from Atmospheric Infrared Sounder/Advanced Microwave Sounding Unit as a function of fractional cloud cover," *J. of Geophys. Res.*, **111**, D09S17, doi:10.1029/2005JD006272 (2006).
- Susskind, J. and O. Reale, "Improving forecast skill by assimilation of AIRS temperature soundings," *Geoscience and Remote Sensing Symp. (IGARSS)*, 2010 IEEE Intl., July 25-30, DOI:10.1109/IGARSS.2010.5652458, 3534-3537 (2010).
- Susskind, J, J. M. Blaisdell, L. Iredell, and F. Keita, "Improved temperature sounding and quality control methodology using AIRS/AMSU data: The AIRS Science Team Version-5 Retrieval Algorithm," *IEEE Trans. on Geoscience and Remote Sens.* **49**, 883-907 doi: 10.1109/TGRS.2010.2070508 (2011).
- Susskind, J., G. Molnar, L. Iredell, and N. G. Loeb, "Interannual variability of outgoing longwave radiation as observed by AIRS and CERES," *J. Geophys. Res.*, **117**, D23107, doi:10.1029/2012JD017997 (2012).
- Susskind, J., J. Blaisdell, and L. Iredell, "Improved methodology for surface and atmospheric soundings, error estimates, and quality control PROCEDURES: THE

- AIRS SCIENCE Team Version-6 retrieval algorithm,” *J. of Applied Rem. Sensing*, 0001; 8(1):084994, doi:10.1117/1.JRS/8/084994 (2014a).
- Susskind, J., J. Lee, and L. Iredell, “Global Distribution and Variability of Surface Skin and Surface Air Temperatures as Depicted in the AIRS Version-6 Data Set”. Presentation at the American Geophysical Union Fall Meeting. Retrieved from the NASA Technical Reports Server: <https://ntrs.nasa.gov/search.jsp?R=20150001442> (2014b).
- Tao, Z., W. J. Blackwell, and D. H. Staelin, “Error variance estimation for individual geophysical parameter retrievals,” *IEEE Trans. Geoscience and Rem. Sens.*, 51, 1718-1727 doi:10.1109/TGRS.2012.2207728 (2013).
- Tretyakov, M., V. V. Parshin, M. A. Koshelev, V. N. Shanin, S. E. Myasnikova, and A. F. Krupnov, 2003: "Studies of 183 GHz water line: broadening and shifting by air, N<sub>2</sub> and O<sub>2</sub> and integral intensity measurements", *J. Molec. Spectros.*, **218**, 239-245.